Evaluating the Lagrangian evolution of subtropical low clouds in GCMs using observations: Mean evolution, timescales, and responses to predictors

Ryan Eastman[1], Christopher R. Terai[2,3], Daniel P. Grosvenor[4], Robert Wood[1]

1. University of Washington, Department of Atmospheric Sciences

2. Department of Earth System Science, University of California, Irvine, CA, USA

3. Lawrence Livermore National Laboratory, Livermore, CA, USA

4. National Centre for Atmospheric Sciences, School of Earth and Environment, University of Leeds, Leeds, LS2 9JT, UK

Corresponding Author Information:

Ryan Eastman

University of Washington Department of Atmospheric Sciences

Box 351640, Seattle WA 98195

Email: rmeast@atmos.washington.edu

Abstract

A Lagrangian framework is developed to show the daily-scale time evolution of low clouds over the Eastern Subtropical Oceans. An identical framework is applied to two General Circulation Models (GCMs): the CAM5 and UKMET and a set of satellite observations. This approach follows thousands of parcels as they advect downwind in the subtropical trade winds, comparing cloud evolution in time and space. This study tracks cloud cover, in-cloud liquid water path (CLWP), droplet concentration (N_d), boundary layer (PBL) depth, and rain rate as clouds transition from regions with predominately stratiform clouds to regions containing mostly trade cumulus.

The two models generate fewer clouds with greater N_d compared to observations. Models show stronger Lagrangian cloud cover decline and greater PBL deepening compared to observations. Comparing frequency distributions of cloud variables over time, models generate increasing frequencies of nearly-clear conditions at the expense of overcast conditions, while observations show transitions from overcast to cloud amounts between 50-90%. Lagrangian decorrelation timescales (e-folding time, τ) of cloud cover and CLWP are between 11 and 19 hours for models and observations, though a bit shorter for models. A Lagrangian framework applied here resolves and compares the time evolution of cloud systems as they adjust to environmental perturbations in models and observations. Increasing subsidence in the overlying troposphere leads to declining cloud cover, CLWP, PBL depth, and rain rates in models and observations. Modeled cloud responses to other meteorological variables are less consistent with observations, suggesting a need for continuing mechanical improvements in GCMs.

1. Introduction

Extensive, warm, low clouds over the eastern subtropical oceans cool the surface by reflecting sunlight while emitting infrared radiation (IR) at a temperature similar to the sea surface. Changes in the properties of these clouds generate large impacts on local and global temperatures (Klein and Hartmann, 1993; Ramanathan et al. 1989; Chen et al 2000). Much effort has gone into understanding the drivers of variability in these clouds to improve their representation in climate models. Currently, General Circulation Models (GCMs) do not consistently simulate realistic low marine clouds, motivating further research into cloud behavior in observations and models (Stephens, 2005). Here we apply a novel Lagrangian approach to two climate models and a set of satellite observations to construct a comparison of daily-scale cloud responses to environmental forcings.

Marine boundary layer clouds in the eastern subtropical oceans form in shallow decks of stratocumulus (Sc) near the west coasts of major continents (Wood 2012). Here, the planetary boundary layer (PBL) is a shallow layer of cool, humid air in contact with a cool sea surface, below a strong temperature and humidity inversion separating the PBL from the relatively warm, dry, and subsiding free troposphere. Air parcels at cloud top cool through upward IR emission, then descend to the sea surface, driving a reciprocating rising. Offshore winds carry these clouds into the tropics while many processes act simultaneously to modify them: Sea surface temperatures (SSTs) warm, imparting latent heat and turbulence, deepening the PBL enough that the radiatively-driven circulation no longer reaches the surface, decoupling the cloud from its moisture source (Wyant et al. 1997). Dry air above the PBL entrains into the cloud, evaporating cloud drops and warming the cloud (Mellado, 2017). Subsidence in the free

troposphere changes: A decrease in subsidence can drive PBL deepening and decoupling (Eastman et al. 2017), while an increase may compress the PBL, lowering the trade inversion to an altitude too shallow to maintain cloud cover within the PBL (Myers and Norris, 2013). Varying moisture and temperature above the PBL modifies the radiative balance at cloud top while altering the evaporative effects of entraining air (Eastman and Wood, 2018). Collision and coalescence of cloud drops can reduce the number concentration of cloud droplets (N_d), changing the cloud properties (Wood et al. 2018). Gravity waves propagating across the PBL erode boundary layer clouds (Yuter et al. 2018). These processes act together on Sc, which are eventually replaced by shallow cumulus (Cu) clouds as they advect into the tropics. This simplified and incomplete list illustrates the challenges facing the modelling communities attempting to create parameterizations in GCMs that simulate the cloud response to their environment.

In Bony and Dufresne (2005), the climatological radiative response of clouds in the tropics to an increase in SST was compared across 15 GCMs, showing inconsistent simulation of shallow marine clouds. Agreement between models and observations was poorest, and the spread between models was greatest, in tropical subsidence regions. This was substantiated by a comparison of 32 models in the Coupled Model Intercomparison Project Phase 5 (CMIP5) by Shin et al. (2017), who show a large inter-model spread in low cloud amounts. Qu et al. (2013) show that the marine cloud response in models is more sensitive to SST than to inversion strength. However, they stress that studying additional environmental variables is necessary.

Nam et al. (2012), comparing within CMIP5, show that models generate too-sparse and too-optically thick clouds compared to observations. They introduce the term ‘too few, too

bright', characterizing the discrepancy, reported more currently by Berry et al. (2019) for the CAM5 model. Karlsson et al. (2010) show that marine boundary layer depths are well represented by models in Sc regions, but downstream there is more model spread and less agreement with data, suggesting differences in parameterizations may be to blame for model spread. Ceppi et al (2017) motivate a strategy to improve cloud behavior in GCMs by introducing cloud resolving models into GCM grid boxes, creating so called superparameterized models, and indeed Parishani et al (2019) have used such a model to examine the cloud response to uniform SST increases, showing significant improvement in the simulation of the vertical PBL structure. Additionally, the DYnamics of the Atmospheric general circulation Modeled On Non-hydrostatic Domains (DYAMOND) project will use models which have a much-improved 3km 'storm-resolving' resolution though they lack the horizontal resolution to resolve PBL eddies. With improvement in computing power, these new models may improve GCM quality, however coinciding observational comparisons will be necessary. This study introduces a new comparison framework for models and observations that will allow for better testing of these parameterizations, focusing on physical mechanisms driving cloud evolution and the cloud system responses to those drivers.

Current studies comparing models to observations often compare averages over several seasons or years, while not addressing day-to-day mechanics. deSzoeke et al. (2016) shows that variability in satellite-observed cloud cover is greatest on multi-day, but sub-seasonal time scales, and that the sensitivity of cloud cover to several environmental predictors varies according to the timescales studied. Compositing techniques, such as those centered on fronts and cyclones presented in Naud et al. (2019) show a great deal of promise in diagnosing model

processes, but they lack a time dimension, which can be used to compare model response times to environmental changes. Eastman et al (2016) shows that e-folding times of cloud cover and cloud liquid water along trajectories are only ~15-18 hours, suggesting cloud response to environmental forcing is strongest on daily time scales. This motivates a new approach to the study of cloud behavior that prioritizes day-to-day mechanics, which can act as a complement to existing techniques and allow for a more complete systematic comparison.

Here we present a framework that can be applied to models and observations in order to assess and compare the responses of cloud variables to environmental forcings on daily timescales. This Lagrangian approach, sampling the same parcels as they evolve in time and space, provides a time dimension, allowing for a more definitive look at cause-and-effect relationships between clouds, their environmental controls, precipitation effects, and aerosol indirect effects which manifest on timescales of hours-to-days. This framework also allows us to compare the cloud response to an unprecedented number of predictors. This study focuses on two GCMs, but future studies can incorporate many more models and predictors.

2. Data

a) Models and observation sources

Two GCMs are compared here: 1) the Community Atmosphere Model (CAM5), and 2) The UK Met office model (abbreviated: UKMET, formally: Hadley Centre Global Environmental Model (HadGEM)). For its physical parameterizations, the Fifth version of the Community Atmosphere Model (CAM5 – Neale et al., 2010) uses the Morrison-Gettelman microphysics

145 scheme of Morrison and Gettelman (2008), the UW shallow cumulus scheme of Park and
146 Bretherton (2009), the turbulence scheme of Bretherton and Park (2009), the deep convection
147 scheme of Zhang and McFarlane (1995), and the RRTMG scheme for radiation (Mlawler et al.,
148 1997; Iacono et al., 2008). A horizontal resolution of ~0.9x1.25° is used with 30 vertical levels.
149 The model is initialized on Jan. 1, 2008 based on ERA-I reanalysis and is left free-running for two
150 years, where the second year of hourly output (2009) is used for this analysis. Monthly SSTs are
151 prescribed by HadISST (Rayner et al. 2003).

152 The UKMET model is the Hadley Centre Global Environmental Model (HadGEM), based
153 upon the Unified Model. The configuration is a hybrid of that used for nested regional
154 simulations (mostly used for numerical weather prediction) and the HadGEM-UKCA
155 configuration used for climate modelling. The main atmospheric components are based on the
156 GA6.1 configuration (Walters et al. 2017) at version 10.3 of the Unified Model, including the
157 UKCA chemistry and aerosols package (Morgenstern 2009, O'Connor 2014).

158 Shallow, mid, and deep convection are parameterized separately in the UKMET from
159 large-scale cloud (Walters et al. 2017) and do not take into account aerosol or droplet number.
160 The large scale cloud microphysics scheme is based on Wilson and Ballard (1999), but with
161 improvements to the warm rain parameterizations (Boutle et al., 2014). The UKCA-Activate
162 scheme is used to produce cloud droplets from aerosol using the West (2014) scheme; this
163 utilizes the parameterization of Abdul-Razzak and Ghan (2000). The bulk properties (cloud
164 fraction, cloud liquid water content, vertical overlap, etc.) of large-scale cloud are
165 parameterized using the prognostic cloud fraction and prognostic condensate (PC2) scheme
166 (Wilson 2008a, Wilson 2008b) with modifications described in Morcrette (2012). The PBL is

parameterized using the turbulence closure scheme of Lock et al. (2000) with modifications described in Lock (2001) and Brown (2008). For radiation, the scheme of Edwards and Slingo (1996) is used with a configuration based on Cusack et al. (1998), but with a number of significant updates as summarized in Walters et al. (2017). A horizontal resolution of ~1.875×1.25° (208×139 km at the equator) is used. Seventy vertical levels are used between the surface and ~70km altitude.

The UKMET model is nudged every 6 hours to ERA-Interim horizontal wind fields between ~2277m and ~47,251m to ensure that the real meteorology is approximately reproduced while allowing fast-acting local boundary layer responses. Following the recommendations of Zhang (2014), we do not nudge the temperature field in order to further allow the model to respond more freely to induced local temperature changes. Instantaneous (non-time averaged) data is output every 7 hours for the UKMET model. Monthly SSTs are prescribed by HadISST, as for the CAM5.

Observational data come from three Afternoon Constellation (A-Train) satellites and the ERA-Interim reanalysis (ERA-I, Dee et al. 2011). The A-Train is a series of sun-synchronous, polar orbiting satellites flying in close formation, sampling the same scenes with a variety of sensors. The A-train crosses the equator at ~1:30 and ~13:30 local time. Model sampling times and locations along trajectories are determined by finding the time and place where the trajectories would have been sampled by the sensors aboard Aqua. Output fields are then interpolated for these times and locations.

b) Lagrangian framework

We compare the behavior of cloud variables as they evolve over 48-hours in the boundary layer along Lagrangian trajectories, driven by the isobaric winds at 925 hPa produced the models and the ERA-Interim reanalysis. Reanalysis winds are used for the observational portion of this work. Model trajectories are generated using the same routine as for the reanalysis winds, substituting model wind fields for reanalysis fields. Study regions include four subtropical ocean basins, first described in Eastman and Wood (2016): The Northeast Pacific, Southeast Pacific, Southeast Atlantic, and the East Indian oceans. The regions are chosen to capture the maximum in Sc near the coasts and the downwind transition into trade Cu, as shown by the climatological averages in Hahn & Warren (2007).

We use a subset of the trajectories introduced in Eastman and Wood (2018), where ~160,000 48-hour forward-running trajectories were computed for 2007-2010. Here, only the years 2009 and part of 2010 are compared. Each trajectory originates from an identical point in the models and observations, chosen at 200-km intervals along the CloudSat/CALIPSO track in order to assess 0-hour precipitation and PBL properties. For the Community Atmosphere Model (CAM5), trajectories are run for the year 2009. For the UK Met Office model, trajectories are run from March 2009-March 2010. Observational trajectories are chosen to overlap with both sets of model trajectories, from January 2009 - March 2010. These time periods do not overlap perfectly, so a test was performed comparing trajectories shared by all three platforms, which showed no qualitative disagreement with the results from the larger sets. Comparisons performed here are based on averages generated by compositing hundreds or thousands of trajectories per platform, not comparing individual trajectories from the same origination point. Cloud and predictor variable samples taken along trajectories include all grid-boxes with

centers within a 100-km radius from each sampling point for both models and observations. We choose this uniform, coarse sampling to even out differences in grid box sizes in source data.

Composited mean trajectories from each model and the reanalysis are compared in Figure 1. This compositing is done by subtracting the starting latitude and longitude from each sample point along each trajectory, then calculating the mean location of all sample points at each sample time within each region, then adding the mean start point from each region to the mean trajectory. All three show comparable mean behavior, with trajectories curving from equatorward to westward. Model trajectories are, on average, slightly longer than the reanalysis trajectories. The geographical distributions of all trajectories from both models and the reanalysis (not shown) show a consistent pattern between all three.

To compare the evolution of trajectories without biases introduced by geographic, seasonal, or diurnal differences, anomalies are generated for all data at all observation times and locations. Anomalies are calculated by subtracting the 100-day running mean at each location sampled, centered on each day, for day and night separately.

Data are broken into two categories: Cloud variables, which describe the nature and amount of cloud cover and depth of the PBL, and predictor variables, which may alter the clouds through a variety of mechanisms.

c) Cloud Variables

Cloud variables are not just a measure of cloud cover, but also water content, droplet concentration, PBL depth, and rain rate. Several of these variables can be measured using a variety of instruments, or can be extracted from models using multiple techniques. Mean

values of these variables are to some extent driven by these procedural differences instead of actual differences between the observations and models. This is an unavoidable drawback of such a study until a truly uniform set of methods is developed, which will be necessary for better comparisons in the future. Although mean values of cloud variables differ, these issues are reduced when assessing Lagrangian change, since the change over time will have the absolute value of a variable removed. For quick reference, observed cloud variables and their sources are briefly described in Table 1, and described in detail below.

i) cloud cover

Cloud cover observations come from the Moderate Resolution Imaging Spectroradiometer (MODIS) level-3 cloud mask product for total cloud cover during day and night (Hubanks et al. 2008; Oreopoulos 2005) from the Aqua satellite. Data are available on a 1°x1° grid. The wide view angle of MODIS causes a zenith angle bias where more cloud cover is reported at wider angles (Maddux et al. 2010). This may cause an observation bias, so a zenith angle correction is applied as described in Eastman and Wood (2016).

Cloud cover data from each GCM is based on the total cloud cover generated by the models within each grid box. A satellite simulator, the Cloud Feedback Model Intercomparison Project (CFMIP) Observation Simulator Package (COSP, Kay & NCAR, 2019) was tested for the UKMET total cloud cover. Cloud amount produced by the COSP was correlated with raw cloud amount, producing a correlation coefficient of r=0.9, meaning variability between the two is nearly equivalent.

ii) Cloud Liquid Water Path

Observations of cloud liquid water path (CLWP) come from the Advanced Microwave Scanning Radiometer for Earth Observing System (AMSR/E, Wentz & Meisner 2004), carried aboard the Aqua satellite. The AMSR/E LWP values represent the total liquid water path (TLWP) for 0.25x0.25° latitude-longitude grid boxes for both clear and cloudy portions. To provide a measurement of in-cloud-only LWP (CLWP), TLWP values are averaged into 1°x1° boxes, then divided by the MODIS cloud fraction in that box.

Liquid water path from AMSR/E may be biased by incorrect partitioning between rain and cloud water (Seethala & Horvath, 2010, Lebsock & Su, 2014). Our AMSR/E CLWP values were compared to those produced by MODIS for daytime-only observations (Platnick et al., 2016), producing a correlation coefficient of r = 0.64 for co-located data points. We use the AMSR/E here because data are available during both day and night. Data from the MODIS CLWP product are used to show the variability between CLWP retrievals from different sensors, but this data is not used in any other analyses.

Liquid water path is output from both GCMs as TLWP, then scaled by model cloud fraction into CLWP. The CAM5 offers a single value of LWP, which may occasionally contain convective clouds. A cloud top height filter was applied, excluding clouds above a range of threshold values, and results were not sensitive to the exclusion/inclusion of occasional convective elements. The UKMET LWP variable is assigned to the cloud-only LWP, excluding rain water and deep convection.

iii) droplet concentration

Cloud droplet number concentration (N_d) is estimated using equation 1 from Eastman and Wood (2016), which is corrected and shown here also as equation 1:

$$N_{eff} = \sqrt{2}\frac{3}{4\pi\rho_\omega}\Gamma_{eff}^{1/2}\frac{LWP^{1/2}}{r_e(h)^3} \quad \text{Equation 1}$$

As in Eastman and Wood 2016: "ρ_ω is the density of liquid water; $\Gamma_{\text{eff}} = \Gamma_{\text{ad}} f_{\text{ad}}$; with Γ_{ad} as a measure of the adiabatic rate of increase in liquid water content with respect to height; constant f_{ad} is an estimate of the degree of adiabaticity; and h represents the cloud top height. We then calculate droplet concentration with the relationship: $N_d = N_{eff}/k$, with *k* assumed to be to 0.8 for marine stratiform clouds (Martin et al. 1994, Wood 2000)". Effective radius (r_e) and LWP come from the daytime-only MODIS 3.7μm retrievals, so N_d is only reported during the day.

Estimating N_d from satellite retrievals requires a significant number of assumptions about the cloud properties (Fu et al. 2019). As for the CLWP mentioned above, two other Nd datasets are compared in order to better show the uncertainty in observed N_d. One dataset comes from Grosvenor & Wood (2018), which uses MODIS collection 5.1 optical retrievals and a different set of assumptions compared to the product described above. The other comes from the regressions described in McCoy et al. (2017) using aerosol concentrations from the Modern-Era Retrospective Analysis for Research and Applications, Version 2 (MERRA-2, Galero et al., 2017).

Cloud droplet number concentrations for cloudy portions of model grid boxes are available for day and night from both models. Cloud-top N_d was derived from CAM5 output for

299 scenes with total cloud fraction greater than 20% and then taking the in-cloud N_d of the upper-
300 most grid box below 350hPa where the cloud fraction is greater than 20%. The CAM5 N_d is very
301 sensitive to the observation level within the cloud, in contrast to N_d behavior in most observed
302 clouds. This routine was necessary to produce physically reasonable CAM5 N_d values. For the
303 UKMET model a weighted vertical mean N_d was calculated, with the liquid water content on
304 each level used for the weights.
305
306 iv) boundary layer depth
307 Observed PBL depths (trade wind inversion height) come from Eastman et al. (2016 &
308 2017). These estimates use the difference between ERA-Interim SSTs and MODIS cloud top
309 temperatures (CTT) of a subset of clouds assumed to sit at the base of the trade inversion using
310 the algorithm described in Eastman et al. (2016). The routine is tuned using the vertical feature
311 mask product from the Cloud-Aerosol Lidar with Orthogonal Polarization (CALIOP) on the
312 Cloud-Aerosol Lidar and Infrared Pathfinder Satellite (CALIPSO, Vaughan et al. 2004) that is co-
313 located in space and time with the MODIS data. Maximum cloud top height (CTH) is also
314 calculated using this routine, but for the coldest cloud top within each box.
315 For the CAM5, PBL depth is estimated as the height below 11 km with maximum
316 vertical-gradient in potential temperature. The PBL depth from the UKMET is assigned to the
317 height at which RH declines most with increasing altitude as shown in Seidel (2010). An
318 approach more comparable to the observations was developed for the UKMET model, where
319 the cloud tops of boundary layer clouds were assumed to rest at the inversion (as diagnosed by
320 the model boundary layer scheme), and this produced a comparable result to the RH method,

correlating with an R value above r = 0.95. Cloud top heights in the CAM5 contained too many outliers above 3km to attempt a similar comparison, so the potential temperature gradient method is used instead.

v) Precipitation

Observed precipitation rate estimates (Average rain rates, Eastman et al. 2019) come from AMSR/E 89 GHz brightness temperatures (T_b, Wentz and Meissner 2004; Ashcroft and Wentz 2006), tuned using CloudSat Rain-Profile rain rates (Stephens et al. 2008; L'Ecuyer and Stephens 2002; Lebsock and L'Ecuyer 2011), AMSR/E column water vapor (CWV) observations (Wentz and Meissner 2004), and ERA5 SSTs and wind speeds (Copernicus Climate Change Service, 2017). The routine from Eastman et al. 2019 was updated for year 2009. This routine relies on the positive relationship between rainfall and warm T_b (Miller and Yuter, 2013) and estimates rain rates from T_b after controlling for confounding variables: SST, CWV, and wind speed.

Precipitation rates in both models are area-average rain rates within each sample. Some UKMET rain rates exceeded the maximum observed rate by several mm/hr. These rates may be an unrealistic model value, or it is possible that the T_b-derived rain rates are not sensitive to rain rates above ~3 mm/hr. In order to improve comparability, UKMET rain rates exceeding the maximum observed rate of 3.1 mm/hr were removed from the analysis, which resulted in the exclusion of less than 0.06% of observations. Rain rates from AMSR/E tuned by CloudSat may also lack sensitivity to extremely light drizzle, or very small cells that do not fill a pixel. This may

bias observed rain towards heavier-precipitating events, but is currently unavoidable given the difficulty in retrieving drizzle rates from satellites.

d) predictor variables

Specific humidity above the PBL is taken at 700 hPa (q_{700}) in both models and in ERA-Interim. Lower Tropospheric Stability (LTS) is the difference in potential temperature (θ) between the surface and 700 hPa in both models and in ERA-Interim. Observed SST comes from the surface skin temperature in ERA-Interim. For the UKMET and CAM5, SST is set to the surface skin temperature, which changes smoothly based on monthly SST data from HadISST (Rayner et al. 2003). Wind speed (WSP) is defined as the 10-meter wind speed, different from the 925 hPa winds driving the trajectories. Ten-meter wind speed was not output in this CAM5 version, which instead offers a wind speed at ~60 meters. The 10-meter winds are estimated using a power law relationship assuming minimal surface roughness and neutral stability, shown in equation 2

$$V_{10m} = V_{60m}\left(\frac{1}{6}\right)^{P} \qquad \text{Equation 2}$$

The wind profile power law exponent P is assumed to be 1/7 (Touma, 1977). V_{10} and V_{60} are wind speeds at 10 and 60 meters, and the ratio between the lower and upper altitudes is 1/6. Subsidence is defined as the pressure velocity at 700 hPa (ω_{700}) for all platforms. Positive ω_{700} is motion moving downward.

3. Methods & Results

a) Mean Lagrangian evolution

The 48-hour Lagrangian evolution of cloud variables are composited in Figure 2. Plots represent the mean of all trajectories in all regions for each platform. The vertical width of each plot represents the 2-σ standard error of the mean. Models produce less cloud cover than observations (Figure 2a), especially the CAM5. Both models show stronger Lagrangian cloud declines than the observations. The MODIS COSP satellite simulated UKMET cloud cover (not shown) produces less daytime cloud cover than the UKMET output cloud variable, suggesting that the true discrepancy between models and observations may be greater. This is likely due to the MODIS instrument missing some small and optically thin clouds. In Figure 2b the UKMET shows more CLWP and the CAM5 shows less than the AMSR/E product used here, though all three show an increase over time. Light gray uncertainty bounds on the observed CLWP plot represent the range of CLWP values produced by the AMSR/E and MODIS, showing a great deal of uncertainty for the absolute values of observed CLWP. Figure 2c shows consistent Lagrangian declines in N_d, with the CAM5 and UKMET producing similar N_d, while observations show less. The light gray error bounds again represent the variability in the absolute values of N_d based on the spread of N_d values produced by the method shown here, the Grosvenor & Wood (2018) N_d, and the McCoy et al. (2017) MERRA-derived value. These wide bounds show a great deal of uncertainty, and suggest that the modeled N_d values fall within the uncertainty bounds produced by these differing methods. The observed PBL is deeper than the CAM5 (Figure 2d), but shallower than the UKMET. Maximum CTH is significantly higher in the CAM5 than in the observations or UKMET, suggesting CAM5 clouds are less sensitive to the inversion, causing

386 excess vertical cloud development instead of horizontal spreading. Modeled PBL depth exhibits
387 more Lagrangian deepening compared to the observations. Rain rates (Figure 2e) are heavier in
388 the CAM5 than in the observations or UKMET. Rain rates increase in both models and the
389 observations, though more strongly in models. Overall, modeled clouds tend to be less
390 extensive and prone to more Lagrangian deepening with stronger increases in rain rates
391 compared to observations.

392 In Figure 3 we compare the mean 48-hour evolution of predictors in the same fashion
393 as Figure 2. Average winds tend to increase slightly in the middle of our trajectories (Figure 3a),
394 then subsequently decline. This wind speed maximum at 24 hours is stronger for the ERA-I,
395 hinting at a possible sampling bias for the observations. However, a diurnal and regional
396 breakdown of these mean winds showed this signal was consistent between regions and for
397 day and night separately. Maps of ERA-I annual mean wind speed show maxima near the
398 downwind edges of our grid boxes, so it is likely that many trajectories are passing through
399 these maxima. The increase in CLWP and rain rate and the decline in N_d at 24-hours in Figure 2
400 may be associated with this wind speed peak, perhaps through modified surface fluxes. Figure
401 3b shows Lagrangian increases in q_{700} for all three plots. The UKMET is drier compared to the
402 nearly equivalent ERA-I and CAM5. The evolution of ω_{700} (Figure 3c), shows the UKMET as an
403 outlier with greater subsidence, despite having the deepest PBL. All three show equivalent
404 Lagrangian declines in subsidence. The Lagrangian evolution of LTS (Figure 3d) shows declines
405 over time for all three curves, and equivalent stability between the ERA-I and UKMET, while the
406 CAM5 is less stable. In Figure 3e SSTs show nearly identical increasing behavior, though the
407 ERA-I shows less of an increase.

A regional breakdown of mean Lagrangian evolution was performed to look for systematic regional biases in models and to see if the differences in mean Lagrangian behavior seen above are due to disagreements everywhere, or just in one region. For the most part, regional variability matched between models and observations with a few exceptions. The PBL in the CAM5 is much deeper than observations in the E Indian, but shallower in the SE Pacific and SE Atlantic. Generally, both model PBLs were deeper and rainier in the E Indian compared to observations. Comparing N_d, the CAM5 has higher N_d in the SE Pacific, perhaps overdoing biomass burning effects there, while the UKMET shows greater N_d in the NE Pacific. Overall, differences are most apparent for droplet concentrations and PBL depths, suggesting that models may have a weaker grasp on those processes.

Normalized frequency distributions of cloud variables are compared at different observation times along trajectories in Figure 4. Distributions are plotted for each variable at three times for all of our trajectories in all regions at T= 0, 24, and 48-hours. Distributions are normalized between 0 and 1 individually for all three sampling times in order to compare the evolution of the shapes of the distributions. Differences are most striking for cloud cover, where both models generate bi-modal distributions, with peaks at around 10% and 100%. In contrast, the observed cloud cover distribution shows a single peak at the overcast end of the x-axis. In observations, the cloud cover distribution gradually shifts from overcast towards broken cloud cover over time, while in models the distribution shifts from overcast to cloud-free. Distributions of CLWP appear similar for all three, though slimmer for the CAM5 and wider for the UKMET. Droplet concentration distributions appear similar for both models and observations, with a single peak, shifted to the right at earlier times. Distributions of PBL depth

show more Lagrangian deepening for the models compared to the observations, but all show a single peak between 1-2 km. For all three platforms, rain rates are usually light with fewer cases of heavier rain.

Differences in the mean values and Lagrangian evolution of cloud variables between models and observations could be explained by a few things. Model variables may be responding too quickly to environmental controls, or cloud variable sensitivity to those controls may be too strong or too weak. The following analyses will test for these possibilities using this Lagrangian framework.

b) Time scales of cloud variables

As clouds evolve following the flow, they are constantly adjusting to perturbations within and surrounding the PBL. Using a Lagrangian framework it is possible to quantify the adjustment times of cloud variables by comparing initial values to subsequent values at a later time. If adjustment timescales of cloud variables are vastly different between models and observations, models may be modifying clouds too quickly or too slowly as the clouds respond to their environment. Disparities in these adjustment timescales could be the cause for differences in the mean behaviors of cloud variables shown above. Here we test for this by comparing characteristic adjustment timescales for cloud variables in models and observations.

These timescales are first explored in Eastman et al. (2016), where cloud variable anomalies (CVAs, as defined in section 2) at later hours are plotted as a function of their 0-hour values. That work shows that, on average, the evolution of anomalies of cloud cover, LWP, N_d, and PBL depth can be modeled as a red noise process with a persistent characteristic

decorrelation timescale: the e-folding time (τ), defined as the time (in hours) that it takes for the lag autocorrelation to decline by a factor of 1/*e*, and is estimated using Equation 3:

$$\tau = \frac{-T}{\log[r(t)]} \qquad \text{Equation 3}$$

Where T is the observation time along the trajectory (T=12, 24, 36, and 48 hours), and *r(T)* is the slope of a line fit to the plot of anomalies at later observation times (y-axis) as a function of the 0-hour anomalies (x-axis). In Eastman et al. (2016) values of τ were on the order of 12-24 hours depending on the variable, showing that CVAs following the flow evolve and respond to environmental perturbations most strongly on daily to sub-daily timescales. In Figures 5-7 we apply that analysis (Eastman et al. 2016, their Figures 6-7) to observed and modeled cloud variables.

Figures 5-7 are made by binning trajectories by their 0-hour CVA into six quantiles (x-axis). The mean CVAs for those quantiles after they evolve along their trajectories are shown on the y-axis as a function of their 0-hour values. For each time T, lines are fit to the plots using a linear regression. Values of τ are calculated using Equation 3 and the slope of each line. As in Eastman et al. (2016), plots for each observation hour are generally linear, though more-so for observations than the models.

For the CAM5 (Figure 5), cloud cover and CLWP behave similarly (5a & b), with τ increasing over time from ~12 to ~18 hours between T=12 and T=48. Values of τ are longer for N_d, PBL depth, and rain rate. N_d shows longer τ at later observation times, ranging from 35 hours to 77 hours, while PBL depth τ increases with observation time from 21 to 27 hours. Rain

474 rates in the CAM5 have a stronger memory at short timescales, with more signal loss at later
475 observation times.

476 UKMET timescales are shown in Figure 6. Timescales for cloud cover and CLWP are again
477 similar to each other and to the CAM5, with τ increasing from ~10 to ~18 from T=12 to T=48.
478 Timescales for N_d and PBL depth are longer, with τ for N_d between 15-29 hours and τ for PBL
479 depth somewhat longer, between 23-35 hours. The precipitation plot appears very noisy with a
480 great deal of uncertainty at times beyond T=12. Rain rates appear to have long memories, but
481 these large numbers appear skewed by a batch of strongly negative initial anomalies that do
482 not diminish in time. In frames a, b, and d the UKMET shows a tendency for initial anomalies on
483 the far end of the negative side to damp out more quickly, skewing the left sides of the plots
484 upward and driving greater uncertainty in the fits. This behavior indicates a tendency in the
485 UKMET to too-quickly damp out negative extremes in cloud fraction, PBL depth, and CLWP.

486 Timescales for observed CVAs are compared in Figure 7. Once again, timescales are
487 shortest for cloud cover and CLWP, increasing from around τ=12-14 to τ=20-21 hours from
488 T=12-48 hours. For N_d, PBL depth, and rain rate, timescales are longer and increase with longer
489 T. Droplet concentration anomalies show τ values between 22-25 hours, while PBL depth shows
490 τ from 16-25 hours and τ for rain rates between 16-21 hours.

491 A comparison of τ at 24 hours for all variables is shown in Table 2. Adjustment
492 timescales for cloud cover and CLWP in models and observations are reasonably comparable,
493 evolving significantly within a diurnal cycle. However, there is a tendency for cloud cover and
494 CLWP in models to evolve more quickly than for observations. These slightly shorter τ values
495 hint at a faster cloud response to evolving environmental forcings in models. This could possibly

explain the faster Lagrangian declines in cloud cover in figure 2. However, this logic fails to explain the more extreme Lagrangian PBL deepening in models since τ values are longer for modeled PBL depth, suggesting that modeled PBL depth evolves more slowly on average. Differences in mean climatological PBL depth behavior may instead be explained by differing sensitivity to environmental forcing. Values of τ for rain rate in both models are longer than in the observations, and the CAM5 τ for N_d is also very long, indicating deficiencies in model rain and microphysical behavior.

c) Effects of Predictor Variables

Cloud evolution can be conceptualized as an internal mechanical system adjusting to a changing environment. Given the ~12-36 hour timescales shown above, the strongest variability in this system is on the order of a single diurnal cycle for both models and observations. Clouds travel hundreds of kilometers in a day, so a Lagrangian framework is necessary to track cloud processes while they occur. In this section we compare observed and modeled cloud responses to predictors while following the flow for one day.

Predictor variables are selected based on how they can act to modify the clouds and the PBL: subsidence acts to press downward on the PBL from above; humid air in the free troposphere emits downwelling IR onto the PBL and mixes into the cloud top through entrainment; LTS modulates entrainment across the inversion through buoyancy differences; changes in SST modify latent and sensible heating into and out of PBL; surface winds mix this heating into the clouds and drive small-scale turbulent circulations. These processes do not all act on the clouds at the same speed, so a test was performed to see whether the initial (0-hour)

values or the 24-hour Lagrangian changes in predictor variable anomalies (PVAs) drove a more powerful CVA response for the observations. Results showed that the 24-hour $\Delta\omega_{700}$ and 24-hour ΔSST were stronger drivers of CVA variability than their 0-hour values, but for all other predictors their 0-hour values were stronger. Therefore, we use the coinciding 24-hour Lagrangian changes in SST and subsidence anomalies as predictors instead of their initial values. Internal cloud processes involve several variables adjusting in concert and modifying one-another, so CVAs are also tested as predictors to show a more complete picture of how clouds respond to their environment and to internal perturbations.

This analysis combines 24-hour trajectory segments containing both day-to-day and night-to-night changes and also combines different regions. To avoid biases associated with combining these trajectories, PVAs and CVAs are used instead of raw values.

To test the effects of predictors, trajectories are subsetted by PVA value into σ bins: $-2<\sigma<-1$, $-1<\sigma<0$, $0<\sigma<1$, and $1<\sigma<2$. We use σ bins in order to compare the power of predictors to one another (e.g. we can compare the change in cloud cover driven by a 1-σ difference in LTS to the change driven by a 1-σ difference in $\Delta\omega_{700}$). The mean 24-hour Lagrangian change in the CVA (ΔCVA, defined as: CVA_{24}-CVA_0) is then calculated for all trajectories within each σ bin.

The ΔCVA is broken into two components as in Eastman et al. (2017) and Eastman and Wood (2018). 1) the change driven by the predictor variable being tested. 2) The change driven by the red noise behavior seen in the prior section and described in Eastman et al. (2016). Section 3b shows that CVAs tend to predictably damp out over time, so a group of trajectories with a mean positive CVA at hour 0 will show a negative change over time, basically a regression to the mean. When we subset trajectories based on predictors, the mean 0-hour

values of CVAs tend to be non-zero (e.g. a set of trajectories with high 0-hour LTS will begin with above-average 0-hour cloud cover). The subsequent mean change in the cloud variable will then be driven by the predictor and by the tendency to regress to the mean. We isolate the change in the CVA driven by the predictor by calculating a residual change, where the change driven by regression to the mean is predicted based on the linear relationships shown in 3b, and is then subtracted from the ΔCVA.

Residual ΔCVA values are produced for each of the four σ bins and the slope of the four points is estimated using a linear regression. This slope represents the mean change in CVA forced by the PVA, independent of red noise. Each predictor variable is tested while another is held constant in bins. The range of slopes produced while holding each other predictor constant produces the uncertainty bounds on the slope. Examples of these slopes are shown in Figures 8 and 9, where the 24-hour residual cloud cover change forced by each predictor is shown for the models and observations. These results are reiterated in Figure 10 and expanded for all predictors.

The slopes in Figure 8 suggest fairly small cloud cover responses to internal cloud variables. Figures 8a and 8c show that cloud decline may be associated with high CLWP and deeper PBLs in both models and observations. The PBL depth appears to be the most consistent predictor, particularly in observations where the entire range of slopes is negative, agreeing with the conclusions of Eastman and Wood (2016), which showed that cloud cover declines in deep PBLs. Ranges of slopes in both models are wide, indicating more uncertainty depending on what is being controlled for.

Figure 9 shows the cloud cover response to meteorological predictors. Here, agreement is seen in frames 9b and c where clouds in both models and the observations decline significantly with increasing ω_{700} and drier q_{700}. Ranges of slopes are all positive in 9b and all negative in 9c, suggesting a great deal of confidence there. Frames 9a and d show that clouds in observations and the UKMET respond positively to stronger surface winds and LTS, while the CAM5 clouds appear less sensitive. Frame 9e shows that both models generate cloud increases when SST increases, but observed clouds show a weak response.

The results from Figures 8 and 9 are reiterated in Figure 10, which represents slopes as bar plots. A positive CVA response to a positive PVA is shown by a bar plot pointing to the right, while a negative response is shown by a bar pointing left. The ranges of slopes shown by the shaded regions of Figures 8 and 9 are shown by horizontal error bars. Figure 10 shows the responses to predictors for cloud cover, CLWP, N_d , PBL depth, and rain rate anomalies. Values of σ (the denominator in the slope calculation) vary between the three platforms. In order to improve equivalence the mean value of σ from all three platforms is used here in the calculation of these slopes, allowing for direct comparison.

Figure 10 presents a great deal of information, so is broken down here by *cloud-modifying-mechanism*. This allows for a systematic comparison of models and observations focused on cloud system processes responding to environmental forcings.

i) Subsidence

Increasing subsidence presses the PBL top downward, reducing PBL depth. This thins existing clouds, as seen by reduced CLWP, and completely dissipates some clouds by pressing

583 the inversion height down below the LCL as shown by the cloud cover response. Models and
584 observations agree on this so far, however the N_d response is different between models and
585 observations: N_d increases in models with increasing subsidence, while it decreases in the
586 observations. This could be an observational issue because thinner, patchier clouds may have
587 more cloud edges in the observation, biasing the N_d low. Conversely, models may overdo the N_d
588 increase due to inadequate parameterizations. Strong rain declines are seen with increasing
589 subsidence in the models. These strong rain responses may have to do with the long
590 decorrelation timescales of model rain. The 24-hour change in rain rate anomaly predicted by
591 red noise in models is small, so a moderate change driven by subsidence may produce a larger
592 residual. Somewhat narrow error bounds on the strong rain response to subsidence shows that
593 rain sensitivity to subsidence occurs independently of other variables, suggesting a somewhat
594 direct rain-subsidence relationship which invites additional scrutiny.
595
596 *ii) PBL deepening driven by radiative cooling*
597 The PBL response to a dry overlying troposphere is different between models and
598 observations. Observations here and in Eastman and Wood (2019) show that the PBL deepens
599 in response to a drier overlying troposphere, as shown by low q_{700}. This deepening is driven by
600 increases in radiative cloud top cooling, which enhances turbulence and entrainment. Both
601 models miss this mechanism, instead showing little PBL sensitivity to q_{700}. This may explain why
602 both models over-deepen the PBL offshore. If the effects of q_{700}, which increases offshore and
603 acts as a brake on PBL deepening, are neglected, clouds will deepen too quickly in the models.
604 The discrepancy may be driven by the reduced cloud cover in the models. Fewer clouds means

605 less surface area emitting IR upward, limiting upward IR flux and reducing cooling and
606 turbulence at PBL top.
607
608 *iii) Entrainment system*
609 The cloud response to higher q_{700} above the PBL is positive in both models and
610 observations. This is likely due to the increased entrainment of water vapor causing less
611 evaporation of cloud drops at cloud top. The unanimous, corresponding increase in CLWP
612 supports this, along with increased rain.
613 Inversion strength also modifies entrainment. Strong inversions are associated with
614 more cloud cover in the observations and UKMET. Both models and observations show that
615 high LTS is associated with less PBL deepening, lower CLWP, and lighter rain. This suggests that
616 the inhibition of entrainment caused by high LTS leads to slower Lagrangian evolution of cloud
617 variables. The CAM5 is an outlier here, showing little cloud cover sensitivity to LTS, which may
618 help to explain the significantly lower CAM5 cloud cover in these regions of climatologically
619 high stability.
620
621 *iv) Cloud microphysics and precipitation*
622 High N_d, which coincides with smaller cloud drop effective radii, inhibits precipitation
623 and leads to persistent clouds (Albrecht et al., 1989; Christensen et al. 2020). Observations here
624 show this, with a negative rain rate response to high N_d and a small corresponding cloud
625 increase. Results show that the cloud response to this system is less powerful compared to
626 some of the others discussed here, but this microphysical mechanism is resolved by the

627 observations. This process is not well simulated in the models, which show little cloud
628 sensitivity to N_d when following the flow. The CAM5 appears to see a decline in precipitation
629 associated with increased N_d, but the rest of this system is absent. Overall, this appears to be an
630 area where models are underperforming. This is surprising, in particular, because previous
631 studies have indicated that the LWP response to aerosols is likely overestimated in climate
632 models (Wang et al., 2012). Additionally, Grosvenor and Carslaw (2020) use a newer version of
633 the UKMET and show that additional aerosol suppresses precipitation and increases clouds in
634 the North Atlantic, though that work did not study Lagrangian change as done here. As
635 mentioned in section 3ci above, this motivates a closer look at model precipitation processes.
636
637 *v. Boundary layer decoupling*
638 The cloud top-to-sea surface circulation is often decoupled in deeper PBLs, cutting off
639 the direct supply of moisture and cloud condensation nuclei to the cloud layer, causing clouds
640 to thin and dry. Observations show this effect with declines seen in cloud cover, N_d, rain rate,
641 and CLWP for trajectories starting in deeper PBLs. The UKMET sees a similar cloud and N_d
642 response, but the CLWP increase in deep PBLs is opposite to the observations. The CAM5
643 produces cloud declines in deeper PBLs, but the N_d and CLWP both appear opposite to the
644 observations, suggesting an incorrect mechanism linking PBL depth and cloud cover evolution
645 there. The CLWP response to deep PBLs is inconsistent between models and observations here,
646 and also shows a great deal of uncertainty. This suggests that models do not properly
647 reproduce the changes in moisture flux into the cloud layer driven by PBL height/decoupling,

possibly indicating shortcomings in simulating thermodynamic processes and lapse rates in the PBL.

vi. Fluxes from surface winds and SST

Stronger wind blowing over warming SST increases moisture and turbulent fluxes in the PBL, invigorating and thickening clouds, and deepening the PBL. All three platforms agree that CLWP is enhanced and the PBL deepens with stronger winds, but models show more PBL deepening compared to observations, while observations show greater increases in cloud cover. A likely explanation is that in models strong winds drive more PBL deepening, so the thicker clouds become more vertically extensive, rather than more horizontally extensive as in the observations.

The cloud cover and N_d responses to ΔSST are strong and positive for both models, but nearly zero for the observations, suggesting the ΔSST is responsible for a greater share of surface fluxes in models than in observations. The PBL deepens in response to a warming SST in the observations and UKMET, but the response leans negative with much uncertainty in the CAM5. Taken together, these analyses suggest that fluxes driven by winds and SST manifest differently in models versus the observations. Modeled cloud cover appears oversensitive to SST changes and under-sensitive to wind speed, while observations show that ΔSST mainly acts on PBL depth with wind speed driving changes to cloud extent.

4. Discussion

a) Model cloud processes and mean behavior

Overall, results above suggest that these models tend to reproduce the subsidence and entrainment-of-humidity mechanisms well. However, the rain rate response to changing subsidence appears overdone in models, which may explain their stronger mean Lagrangian increase in rainfall, possibly overreacting to the mean decline in subsidence. The UKMET successfully simulates the effects of LTS on cloud variable evolution, though still shows less cloud cover sensitivity than observations. Cloud cover in the CAM5 shows no sensitivity to LTS. The weaker or nonexistent sensitivity of modeled clouds to LTS may explain the reduced cloud cover in these study regions, which are characterized by strong inversions. Further, the stronger Lagrangian reduction in model cloud cover could be explained by the lack of sensitivity to LTS and to faster characteristic timescales, allowing modeled cloud variables to evolve more quickly.

These results showing strong cloud declines associated with increased subsidence add to those from Myers and Norris (2013), which show that clouds are less extensive with enhanced subsidence when LTS is kept constant. This work shows that model clouds respond to subsidence changes quickly and strongly, indicating that the downwind gradient of subsidence will be of great importance to cloud evolution along with the mean value of subsidence. New studies should take into account the changing subsidence gradient in these regions. It is encouraging that both models simulate the subsidence system well, adding credibility to the cloud response to weakening subsidence in global warming scenarios. Improvement in the LTS-cloud relationships motivated here should further aid in simulating the cloud response to global warming.

692 Differences between the Lagrangian evolution of CLWP between the models and
693 observations are apparent in Figure 2, where the UKMET shows significantly more CLWP, but
694 less cloud cover than the observations. The results of Figure 10 show that UKMET CLWP is much
695 more sensitive to nearly all predictors compared to the CAM5, and to some extent more
696 sensitive than the observations. This hints at a system in the UKMET that tends to strongly
697 modify cloud water, but not cloud extent. The CAM5 CLWP, meanwhile, tends to be less
698 sensitive to predictors than the UKMET or observations, and also shows the least CLWP in
699 Figure 2.
700 Models are less consistent with observations for a variety of other mechanisms. Both
701 models miss the radiative effects of overlying humidity on PBL deepening, possibly contributing
702 to the increased climatological Lagrangian deepening seen in models compared to
703 observations.
704 Processes internal to the PBL may contribute to discrepancies in mean behavior, though
705 their linkage to differences seen in Figure 2 are less clear. Models appear to miss aerosol-cloud-
706 precipitation processes when viewed from the Lagrangian reference frame. The aerosol-cloud-
707 lifetime effect appears absent in both models. Further, in many places the response of N_d to
708 predictors disagrees between models and observations. This appears to be a particular
709 weakness in these models, and suggests that further improvements in model microphysics may
710 aid in their performance. Deepening-decoupling processes in the PBL are partially well
711 represented, with clouds breaking up in deep PBLs for all three platforms. However, the
712 coinciding CLWP and N_d behaviors show less agreement, hinting at possible shortcomings in
713 model-produced thermodynamic processes or surface fluxes. The UKMET in particular seems to

increase CLWP in deep boundary layers, perhaps failing to properly decouple the cloud from surface moisture sources. It seems likely that the path from sea surface to cloud is not well simulated in models, where clouds are oversensitive to SST and under-sensitive to wind speed. These internal processes need further study in isolation in order to assess their effects on the mean behavior of modeled clouds. It will be necessary to simulate these processes correctly in order to predict systematic cloud responses to climate changes

b) Differences in Variables

Due to observational limitations not all model output variables can be easily compared with observations. This is particularly a problem for measurements of CLWP, N_d, and PBL depth. These inconsistencies drive the need for model variables that can be compared more directly with observations in order to eliminate the discrepancies caused by observational issues rather than physical behavior. These discrepancies may partially cause the disagreements seen in Figure 2. Continuing improvements in satellite simulators for GCM output will go a long way towards improving these comparisons. Furthermore, sensor and observation technique improvements will hopefully shrink the wide ranges of variability seen in observations from different sensors in Figures 2b and 2c.

c) Future work

The framework presented here can be applied to a limitless number of GCMs in order to test for consistency between models and observations. Future work seeks to streamline our process so that modeling groups can generate trajectories and variables from their model

output. By focusing on cloud mechanics on daily timescales, and using a time dimension to directly assess causality, this Lagrangian framework can add value and show which cloud processes are well simulated and which are lacking. Additional comparisons with global cloud-resolving models may help us discern whether cloud responses are controlled by poorly resolved processes. Further, a comparison should be made between a free-running model and the same model with winds nudged by reanalysis fields, hopefully discerning whether cloud responses are due to differing meteorology or model mechanics.

5. Conclusions

This Lagrangian analysis compares the time evolution of clouds and cloud variables in several ways. Results appear consistent with the "too few, too bright" issues mentioned in other work with models producing higher N_d and less cloud cover. Cloud tops in the CAM5 appear to overshoot the trade inversion by several kilometers, while the observations and UKMET model do not show such extreme vertical development in the subtropics. Lagrangian tendencies of cloud variables and predictor variables are more consistent between platforms, though Lagrangian cloud cover decline and PBL deepening are stronger in the two models than in the observations. A comparison of the time evolution of predictors shows behavior consistent with a transition from a subtropical Sc to a tropical trade Cu environment, with declines in LTS and subsidence and increases in SST.

The time evolution of frequency distributions of cloud cover shows that both models generate bimodal distributions of cloud cover with peaks at overcast and below 25% cloud

757 cover. At later times the models tend to increase cloud amounts at the low peak. Observations
758 disagree, showing distributions that tend to change from overcast to merely broken scenes.
759 Despite the differences in the evolution of frequency distributions, the characteristic
760 timescales of cloud cover and CLWP, represented by the e-folding time (τ), shows some
761 consistency between both models and observations. For all three, cloud cover and CLWP have
762 shorter τ, between 11-19 hours, compared to PBL depth, N_d, and rain rates, which were
763 consistently longer in models than observations, though showing more noise and significantly
764 less consistency between platforms.
765 Finally, a comparison of responses to predictors shows that cloud cover and cloud
766 variables in all three platforms are consistently and powerfully affected by $\Delta\omega_{700}$. Increasing
767 ω_{700} drives declines in cloud cover, CLWP, PBL depth, and rain rate. This is opposite from the
768 evolution of the mean state of the Sc-Cu transition where subsidence decreases as clouds
769 decrease, thus this approach allows us to isolate impacts of predictors and test model
770 responses in a way that is not possible using the mean trajectories alone. Free tropospheric
771 humidity drives increases in cloud cover and CLWP for all three platforms, however models do
772 not show that a drier overlying troposphere can lead to PBL deepening, which is shown in
773 observations. Discrepancies in the cloud and cloud variable responses to other meteorological
774 forcings and to internal variables suggests that cloud mechanics are not yet accurately
775 represented in the models, with inconsistent responses to wind speed, SST, and PBL depth. This
776 framework can be applied to any number of climate models in the future to diagnose
777 shortcomings in cloud simulations and compare free-running climate models with those nudged
778 by reanalysis winds.

Acknowledgements: RE was supported by NASA CloudSat and CALIPSO Science Team award 80NSSC19K1274.

DPG was funded from the National Environment Research Council (NERC) funded “North Atlantic Climate System: integrated Study (ACSIS)'' project via NCAS, grant number NE/N018001/1. We acknowledge use of the MONSooN system, a collaborative facility supplied under the Joint Weather and Climate Research Programme, a strategic partnership between the Met Office and the Natural Environment Research Council.

CRT's work was supported by the Exascale Computing Project(17-SC-20-SC), and conducted under the auspices of the U.S. Department of Energy by Lawrence Livermore National Laboratory under Contract DE-AC52-07NA27344. This research used resources of the National Energy Research Scientific Computing Center(NERSC), a U.S. Department of Energy Office of Science User Facility operated under Contract DE-AC02-05CH11231.

Analysis scripts used to process model data can be found at:

https://github.com/crterai/LagrangianAnalysis

Data Availability

ERA Interim data used here are available at: https://**doi**.org/10.1002/qj.828. As in Dee et al. 2011.

ERA5 data (**DOI**: 10.5065/D6X34W69) used are available at: https://apps.ecmwf.int/data-catalogues/era5/?class=ea

MODIS collection 6 L3 data are available at: http://dx.doi.org/10.5067/MODIS/MYD08_D3.006

AMSR/E L3 gridded day and night averages from Wentz et al. 2014 are available at: www.remss.com/missions/amsr

AMSR/E 89 GHz Brightness temperatures from Ashcroft and Wentz (2006) are available at: https://doi.org/10.5067/YL62FUZLAJUT

CloudSat Rain-Profile (Lebsock and L'Ecuyer, 2011) Data are made available here: http://www.cloudsat.cira.colostate.edu/data-products/level-2c/2c-rain-profile

CALIPSO Vertical Feature Mask data are available: https://eosweb.larc.nasa.gov/project/calipso/lidar_l2_vfm_table

The observed PBL and rain rate estimate data are processed using the above datasets and are also available from the author upon request. Rain rates should be publicly available when the data finish processing in mid-2020.

References

Abdul-Razzak, H., and S. J. Ghan, 2000: A parameterization of aerosol activation: 2. Multiple aerosol types. *J. Geophys. Res.*, **105**, 6837–6844, https://doi.org/10.1029/1999JD901161.

Albrecht, B. A., 1989:. Aerosols, Cloud Microphysics, and Fractional Cloudiness. *Science*, **245** (4923), 1227-1230. doi: 10.1126/science.245.4923.1227

Ashcroft, P., and F. Wentz, 2006: AMSR-E/Aqua L2A global swath spatially-resampled brightness temperatures, version 2. National Snow and Ice Data Center, Accessed: October 2017.

Berry, E., G. G. Mace, and A. Gettleman, 2019: Using A-Train Observations to Evaluate Cloud Occurrence and Radiative Effects in the Community Atmosphere Model during the Southeast Asia Summer Monsoon. *J. Climate*, **32**, 4145-4165.

Bony, S., and J.-L. Dufresne, 2005: Marine boundary layer clouds at the heart of tropical cloud feedback uncertainties in climate models. *Geophys. Res. Lett.,* **32**, L20806.

Boutle, I. A., S. J. Abel, P. G. Hill, and C. J. Morcrette, 2014: Spatial variability of liquid cloud and rain: observations and microphysical effects, *Q. J. Roy. Meteorol. Soc*., **140**, 583–594, https://doi.org/10.1002/qj.2140.

Bretherton, C. S. and S Park, 2009: A new moist turbulence parameterization in the Community Atmosphere Model. *J. Climate*, **22**, 3422-3448.

Brown, A. R., R. J. Beare, J. M. Edwards, A. P. Lock, S. J. Keogh, S. F. Milton, and D. N. Walters, 2008: Upgrades to the boundary-layer scheme in the Met Office numerical weather prediction model, *Bound.-Lay. Meteorol.,* **128**, 117–132, https://doi.org/10.1007/s10546-008-9275-0.

Ceppi, P., F. Brient, M. D. Zelinka, and D. L. Hartmann, 2017: Cloud feedback mechanisms and their representation in global climate models. *Wiley Interdiscip. Rev.: Climate Change*, **8**, e465.

Chen, T., W. B. Rossow, and Y. C. Zhang, 2000: Radiative effects of cloud-type variations. *J. Climate*, **13**, 264–286.

Christensen, M. W., Jones, W. K., and P. Stier, 2020: Aerosols enhance cloud lifetime and brightness along the stratus-to-cumulus transition. *PNAS*, **117** (30), 17591-17598; https://doi.org/10.1073/pnas.1921231117

Copernicus Climate Change Service (C3S), 2017: ERA5: Fifth generation of ECMWF atmospheric reanalyses of the global climate . Copernicus Climate Change Service Climate Data Store (CDS), Accessed: December, 2019. https://cds.climate.copernicus.eu/cdsapp#!/home

Cusack, S., A. Slingo, J. M. Edwards, and M. Wild, 1998: The radiative impact of a simple aerosol climatology on the Hadley Centre atmospheric GCM*, Q. J. Roy. Meteorol. Soc*., 1**24**, 2517–2526, https://doi.org/10.1002/qj.49712455117,

de Szoeke, S. P. and K. L. Verlinden, 2016: The time scales of variability of marine low clouds. *J. Climate*, **29**, 6463-6481.

Dee, D. P., and Coauthors, 2011: The ERA-Interim reanalysis: Configuration and performance of the data assimilation system. *Quart. J. Roy. Meteor. Soc*., **137**, 553–597.

Diamond, M. S., A. Dobracki, S. Freitag, J. D. Small Griswold, A. Heikkila, S. G. Howell, M. E. Kacarab, J. R. Podolske, P. E. Saide, and R. Wood, 2018: Time-dependent entrainment of smoke presents an observational challenge for assessing aerosol–cloud interactions over the southeast Atlantic Ocean, *Atmos. Chem. Phys*., **18**, 14623–14636, https://doi.org/10.5194/acp-18-14623-2018.

Eastman, R. and R. Wood, 2016: Factors controlling low-cloud evolution over the eastern subtropical oceans: A Lagrangian perspective using the A-Train Satellites. *J. Atmos. Sci.,* **73**, 331-351.

Eastman, R., R. Wood, and C. S. Bretherton, 2016: Time scales of clouds and cloud-controlling variables in subtropical stratocumulus from a Lagrangian perspective. *J. Atmos. Sci*., **73**, 3079-3091.

Eastman, R., R. Wood, and K. T. O, 2017: The subtropical stratocumulus-topped planetary boundary layer: a climatology and the Lagrangian evolution*. J. Atmos. Sci*., **74**, 2633-2656.

Eastman R. and R. Wood, 2018: The competing effects of stability and humidity on subtropical stratocumulus entrainment and cloud evolution from a Lagrangian perspective. *J. Atmos Sci.* **75**(8), 2563–78.

Eastman R., Lebsock, M., and R. Wood, 2019: Warm Rain Rates from AMSR-E 89-GHz Brightness Temperatures Trained Using CloudSat 380 Rain-Rate Observations. *Journal of Atmospheric and Oceanic Technology,* **36**, 1033–1051.

Edwards, J. M. and A. Slingo, 1996: Studies with a flexible new radiation code. I: Choosing a configuration for a large-scale model, *Q. J. Roy. Meteorol. Soc*., **122**, 689–719, https://doi.org/10.1002/qj.49712253107.

911 Galero, R., and coauthors, 2017: The Modern-Era Retrospective Analysis for Research and
912 Applications, Version 2 (MERRA-2), *J. Climate*, **30** (14), 5419–5454, doi: 10.1175/JCLI-D-
913 16-0758.1
914
915 Grosvenor, D. P., & Wood, R., 2018: Daily MODIS (MODerate Imaging Spectroradiometer)
916 derived cloud droplet number concentration global dataset for 2003-2015. *Centre for*
917 *Environmental Data Analysis,* January, 2020.
918
919 Grosvenor, D. P. and K. S. Carslaw, 2020: How does the UKESM1 climate model produce its
920 cloud-aerosol forcing in the North Atlantic?, *Atmos. Chem. Phys.,*
921 https://doi.org/10.5194/acp-2020-502
922
923 Hahn, C. J. and S. G. Warren, 2007: A gridded climatology of clouds over land (1971-96) and
924 ocean (1954-97) from surface observations worldwide. Numeric Data Package NDP-026E
925 ORNL/CDIAC-153, CDIAC, Department of Energy, Oak Ridge, Tennessee.
926
927 Hubanks, P. A., M. D. King, S. Platnick, and R. Pincus, 2008: MODIS Atmosphere L3 gridded
928 product algorithm theoretical basis document. MODIS Tech. Doc. ATBD-MOD-30, 96 pp.
929
930 Iacono, M. J., J. S. Delamere, E. J. Mlawer, M. W. Shephard, S. A. Clough, and W.
931 D. Collins, 2008: Radiative forcing by long-lived greenhouse gases: Calculations with the
932 AER radiative transfer models. *J. Geophys. Res.*, **113**, D13103.
933
934 Karlsson, J., G. Svensson, S. Cardoso, J. Teixeira, and S. Paradise, 2010: Subtropical cloud-regime
935 transitions: Boundary layer depth and cloud-top height evolution in models and
936 observations. *J. Appl. Met. and Clim.,* **49**, 1845-1858.
937
938 Kay, J. & National Center for Atmospheric Research Staff (Eds), 2019: "The Climate Data Guide:
939 COSP: Cloud Feedback Model Intercomparison Project (CFMIP) Observation Simulator
940 Package." Retrieved from https://climatedataguide.ucar.edu/climate-data/cosp-cloud-
941 feedback-model-intercomparison-project-cfmip-observation-simulator-package.
942
943 King, M. D., and Coauthors, 2003: Cloud and aerosol properties, precipitable water, and profiles
944 of temperature and humidity. *IEEE Trans. Geosci. Remote Sens*., **41**, 442–458.
945
946 Klein S. A., and D. L. Hartmann, 1993: The seasonal cycle of low stratiform clouds. *J. Clim*., **6**,
947 1587–1606.
948
949 Klein, S. A., A. Hall, J. R. Norris, and R. Pincus, 2017: Low-cloud feedbacks from cloud-controlling
950 factors: A review. *Surveys in Geophysics*, **38**(6), 1307-1329.
951
952 L'Ecuyer, T. S., and G. L. Stephens, 2002: An estimation-based precipitation retrieval algorithm
953 for attenuating radars. *J. Appl. Meteor*., **41**, 272–285.
954

Lebsock, M. D., and T. S. L'Ecuyer, 2011: The retrieval of warm rain from CloudSat. *J. Geophys. Res.*, **116**, D20209.

Lebsock, M. D., & H. Su, 2014: Application of active spaceborne remote sensing for understanding biases between passive cloud water path retrievals, **119**, 1–18. https://doi.org/10.1002/2014JD021568.

Lock, A. P., 2001: The numerical representation of entrainment in parametrizations of boundary layer turbulent mixing, *Mon. Weather Rev.,* **129**, 1148–1163, https://doi.org/10.1175/1520-0493(2001)129<1148:TNROEI>2.0.CO;2.

Lock, A. P., A. R. Brown, M. R. Bush, G. M. Martin, and R. N. B. Smith, 2000: A new boundary layer mixing scheme. Part I: Scheme description and single-column model tests, *Mon. Weather Rev.*, **128**, 3187–3199, https://doi.org/10.1175/1520-0493(2000)128<3187:ANBLMS>2.0.CO;2.

Maddux, B. C., S. A. Ackerman, and S. Platnick, 2010: Viewing geometry dependencies in MODIS cloud products. *J. Atmos. Oceanic Technol.,* **27**, 1519-1528.

Martin, G. M., D. W. Johnson, and A. Spice, 1994: The measurement and parameterization of effective radius of droplets in warm stratocumulus clouds. *J. Atmos. Sci*., **51**, 1823-1842.

McCoy, D. T., F. A. M. Bender, J. K. C., Mohrmann, D. L. Hartmann, R. Wood, and D. P. Grosvenor, 2017: The global aerosol-cloud first indirect effect estimated using MODIS, MERRA and AeroCom, *J. Geophys. Res.-Atmos*., 1779–1796, https://doi.org/10.1002/2016JD026141.

Mellado, J. P., 2017: Cloud-top entrainment in stratocumulus clouds. *Annu. Rev. Fluid Mech.*, **49**, 145–169

Miller, M. A., and S. E. Yuter, 2013: Detection and characterization of heavy drizzle cells within subtropical marine stratocumulus using AMSR-E 89-GHz passive microwave measurements. *Atmos. Meas. Tech.,* **6**, 1–13.

Mlawer, E. J., S. J. Taubman, P. D. Brown, M. J. Iacono, and S. A. Clough, 1997: Radiative transfer for inhomogeneous atmospheres: RRTM, a validated correlated-k model for the longwave. *J. Geophys. Res.*, **102**, 16 663–16 682

Morcrette, C. J., 2012: Improvements to a prognostic cloud scheme through changes to its cloud erosion parametrization, *Atmos. Sci. Let*., **13**, 95–102, https://doi.org/10.1002/asl.374.

997 Morgenstern, O., P. Braesicke, F. M. O'Connor, A. C. Bushell, C. E. Johnson, S. M. Osprey, and J.
998 A. Pyle, 2009: Evaluation of the new UKCA climate-composition model – Part 1: The
999 stratosphere, *Geosci. Model Dev.,* **2**, 43–57, https://doi.org/10.5194/gmd-2-43-2009.
1000
1001 Morrison, H., and A. Gettelman, 2008: A new two-moment bulk stratiform cloud microphysics
1002 scheme in the Community Atmosphere Model, version 3 (CAM3). Part I: Description and
1003 numerical tests. *J. Climate*, **21**, 3642-3659. doi:10.1175/2008JCLI2105.1
1004
1005 Myers, T. A. and J. R. Norris, 2013: Observational evidence that enhanced subsidence reduces
1006 subtropical marine boundary layer cloudiness. *J. Climate*, **26** (19), 7507–7524.
1007
1008 Nam, C., S. Bony, J.-L. Dufresne, and H. Chepfer, 2012: The 'too few, too bright' tropical low-
1009 cloud problem in CMIP5 models, *Geophys. Res. Lett.*, **39**, L21801.
1010
1011 Naud, C. M., J. F. Booth, J. Jeyaratnam, L. J. Donner, C. J. Seman, M. Zhao, H. Guo, and Y. Ming,
1012 2019: Extratropical Cyclone Clouds in the GFDL Climate Model: Diagnosing Biases and
1013 the Associated Causes. *J. Climate*, **32**, 6685–6701, https://doi.org/10.1175/JCLI-D-19-
1014 0421.1.
1015
1016 Neale, R. B., et al., 2010: Description of the NCAR Community Atmosphere Model
1017 (CAM5.0), *NCAR Tech. Note NCAR/TN-486+STR* , Natl. Cent. for Atmos. Res., Boulder,
1018 Colo. [Available at http://www.cesm.ucar.edu/models/cesm1.0/cam/.]
1019
1020 O'Connor, F. M., C. E. Johnson, O. Morgenstern, N. L. Abraham, P. Braesicke, M. Dalvi, G. A.
1021 Folberth, M. G. Sanderson, P. J. Telford, A. Voulgarakis, P. J. Young, G. Zeng., W. J.
1022 Collins, and J. A. Pyle, 2014: Evaluation of the new UKCA climate-composition model –
1023 Part 2: The Troposphere, *Geosci. Model Dev.,* **7**, 41–91, https://doi.org/10.5194/gmd-7-
1024 41-2014.
1025
1026 Oreopoulos, L., 2005: The impact of subsampling on MODIS level-3 statistics of cloud optical
1027 thickness and effective radius. IEEE Trans. *Geosci. Remote Sens*., **43**, 366–373.
1028
1029 Parishani, H., M. S. Pritchard, C. S. Bretherton, M. C. Wyant, and M. Khairoutdinov, 2019:
1030 Toward low-cloud-permitting cloud superparameterization with explicit boundary layer
1031 turbulence. *Journal of Advances in Modeling Earth Systems*, **9**, 1542– 1571.
1032
1033 Park, S., and C. S. Bretherton, 2009: The University of Washington shallow convection scheme
1034 and moist turbulence schemes and their impact on climate simulations with the
1035 Community Atmosphere Model. *J. Climate*, **22,** 3449–3469.
1036
1037 Platnick, S., et al., 2016: The MODIS cloud optical and microphysical products: Collection 6
1038 updates and examples from Terra and Aqua, *IEEE Trans. Geosci. Remote Sens.,* **55**, 1,
1039 502-525.
1040

Qu, X., A. Hall, S. Klein, P. M. Caldwell, 2014: On the spread of changes in marine low cloud ocver in climate model simulations of the 21st century. *Clim. Dyn.*, **42**, 2603-2626

Ramanathan, V., R. D. Cess, E. F. Harrison, P. Minnis, B. R. Barkstrom, E. Ahmed, and D. L. Hartmann, 1989: Cloud-radiative forcing and climate: results from the Earth radiation budget experiment. *Science*, **243**(4887), 57-63.

Rayner, N. A., D. E. Parker, E. B. Horton, C. K. Folland, L. V. Alexander, D. P. Rowell, E. C. Kent, A. Kaplan, 2003: Global analyses of sea surface temperature, sea ice, and night marine air temperature since the late nineteenth century, *J. Geophys. Res.*, **108**, D14, 4407 10.1029/2002JD002670.

Seethala, C. and Á, Horváth, 2010: Global assessment of AMSR-E and MODIS cloud liquid water path retrievals in warm oceanic clouds. *J. Geophys. Res.,* **115**, D13202.

Seidel, D. J., C. O. Ao, and K. Li, 2010: Estimating climatological planetary boundary layer heights from radiosonde observations: Comparison of methods and uncertainty analysis. *J. Geophys. Res*., **115**, D16113.

Shin, S.-H., O.-Y. Kim, D. Kim, and M.-I. Lee, 2017: Cloud radiative effects and changes simulated by the coupled model intercomparison project phase 5 models. *Advances in Atmospheric Sciences,* **34**, 859-876.

Stephens, G. L. et al., 2008: The CloudSat mission: Performance and early science after the first year of operation. *J. Geophys. Res*. **113**, D00A18.

Stephens, G. L., 2005: Cloud feedbacks in the climate system: A critical review. *J. Climate*, **18**, 237–273.

Touma, J. S., 1977: Dependence of the Wind Profile Power Law on Stability for Various Locations, *Journal of the Air Pollution Control Association*, **27** (9), 863-866.

Vaughan, M., S. Young, D. Winker, K. Powell, A. Omar, Z. Liu, Y. Hu, and C. Hostetler, 2004: Fully automated analysis of space-based lidar data: an overview of the CALIPSO retrieval algorithms and data products. *SPIE Int. Soc. Opt. Eng.*, **5575**, 16-30.

Walters, D. and coauthors, 2017: The Met Office Unified Model Global Atmosphere 6.0/6.1 and JULES Global Land 6.0/6.1 configurations, *Geosci. Model Dev*., **10**, 1487–1520, https://doi.org/10.5194/gmd-10-1487-2017.

Wang, M., et al., 2012: Constraining cloud lifetime effects of aerosols using A-Train satellite observations. *Geophysical Research Letters*, **39** (15). doi: 10.1029/2012GL052204

Wentz, F. J. and T. Meissner. 2004: AMSR-E/Aqua L2B Global Swath Ocean Products derived from Wentz Algorithm. Version 2. [L3 LWP]. Boulder, Colorado USA.

Wentz, F. J., T. Meissner, C. Gentemann, M. Brewer, 2014: Remote Sensing Systems AQUA AMSR-E [Daily] Environmental Suite on 0.25 deg grid, Remote Sensing Systems, Santa Rosa, CA. Available online at www.remss.com/missions/amsr

West, R. E. L., P. Stier, A. Jones, C. E. Johnson, G. W. Mann, N. Bellouin, D. G. Partridge, and Z. Kipling, 2014: The importance of vertical velocity variability for estimates of the indirect aerosol effects, *Atmos. Chem. Phys*., **14**, 6369–6393, https://doi.org/10.5194/acp-14-6369-2014.

Wilson, D. R. and S. P. Ballard, 1999: A microphysically based precipitation scheme for the UK Meteorological Office Unified Model, *Q. J. Roy. Meteorol. Soc*., **125**, 1607–1636, https://doi.org/10.1002/qj.49712555707.

Wilson, D. R., A. C. Bushell, A. M. Kerr-Munslow, J. D. Price, and C. J. Morcrette, 2008a.: PC2: A prognostic cloud fraction and condensation scheme. I: Scheme description, *Q. J. Roy. Meteorol. Soc.*, **134**, 2093–2107, https://doi.org/10.1002/qj.333.

Wilson, D. R., A. C. Bushell, A. M. Kerr-Munslow, J. D. Price, C. J. Morcrette, and A. Bodas-Salcedo, 2008b: PC2: A prognostic cloud fraction and condensation scheme. II: Climate model simulations, *Q. J. Roy. Meteorol. Soc.,* **134**, 2109-2125, https://doi.org/10.1002/qj.332.

Wood, R., 2000: Parametrization of the effect of drizzle upon the droplet effective radius in stratocumulus clouds. *Q. J. R. Meteorol. Soc*., **126**, 3309-3324.

Wood, R., 2012: Stratocumulus clouds. *Mon. Wea. Rev*., **140**, 2373-2423.

Wood, R., and Coauthors, 2018: Ultraclean layers and optically thin clouds in the stratocumulus to cumulus transition. Part I: Observations. *J. Atmos. Sci.*, **75**, 1631–1652.

Wyant, M. C., C. S. Bretherton, H. A. Rand, and D. E. Stevens, 1997: Numerical simulations and a conceptual model of the stratocumulus to trade cumulus transition. *J. Atmos. Sci*., **54**, 168-192.

Yuter, S. E., J. D. Hader, M. A. Miller, and D. B. Mechem, 2018: Abrupt cloud clearing of marine stratocumulus in the subtropical southeast atlantic. *Science*, **361**(6403), 697-701.

Zhang, G. J. and N. A. McFarlane, 1995: Sensitivity of climate simulations to the parameterization of cumulus convection in the Canadian climate centre general circulation model, *Atmosphere-Ocean*, **33:3**, 407-446.

Zhang, K., H. Wan, X. Liu, S. J. Ghan, G. J. Kooperman, P.-L. Ma, P. J. Rasch, D. Neubauer, and U. Lohmann, 2014: Technical Note: On the use of nudging for aerosol–climate model intercomparison studies, *Atmos. Chem. Phys.,* **14**, 8631–8645, https://doi.org/10.5194/acp-14-8631-2014.

Tables

Cloud Variable	Data Source (observations)
Cloud	MODIS C6 L3 cloud mask
CLWP	AMSR/E L3 LWP
Nd	From MODIS c6 optical properties re and lwp, as in Eastman & Wood (2016)
PBL	MODIS C6 CTT - ERA-I SST, tuned using CALIPSO VFM, using Eastman et al. (2016) routine
Rain	AMSR/E 89 GHz Tb, trained using CloudSat

Table 1. A brief list of observed cloud variable sources.

24-hr τ	CAM5	UKMET	OBS
Cloud Cover	15.9	13.4	19.4
CLWP	16.3	13.3	17.5
Nd	57.7	22	21.7
PBL depth	27.1	30.8	23.8
Rain Rate	43.7	66.4	20.2

Table 2. e-folding times (τ) estimated using the (red, 24-hour) slopes in Figures 5-7 and Equation 3. Values of τ represent the time in hours for the lag autocorrelation for a cloud variable to decline by a factor of 1/e as it evolves following the flow.

Figures

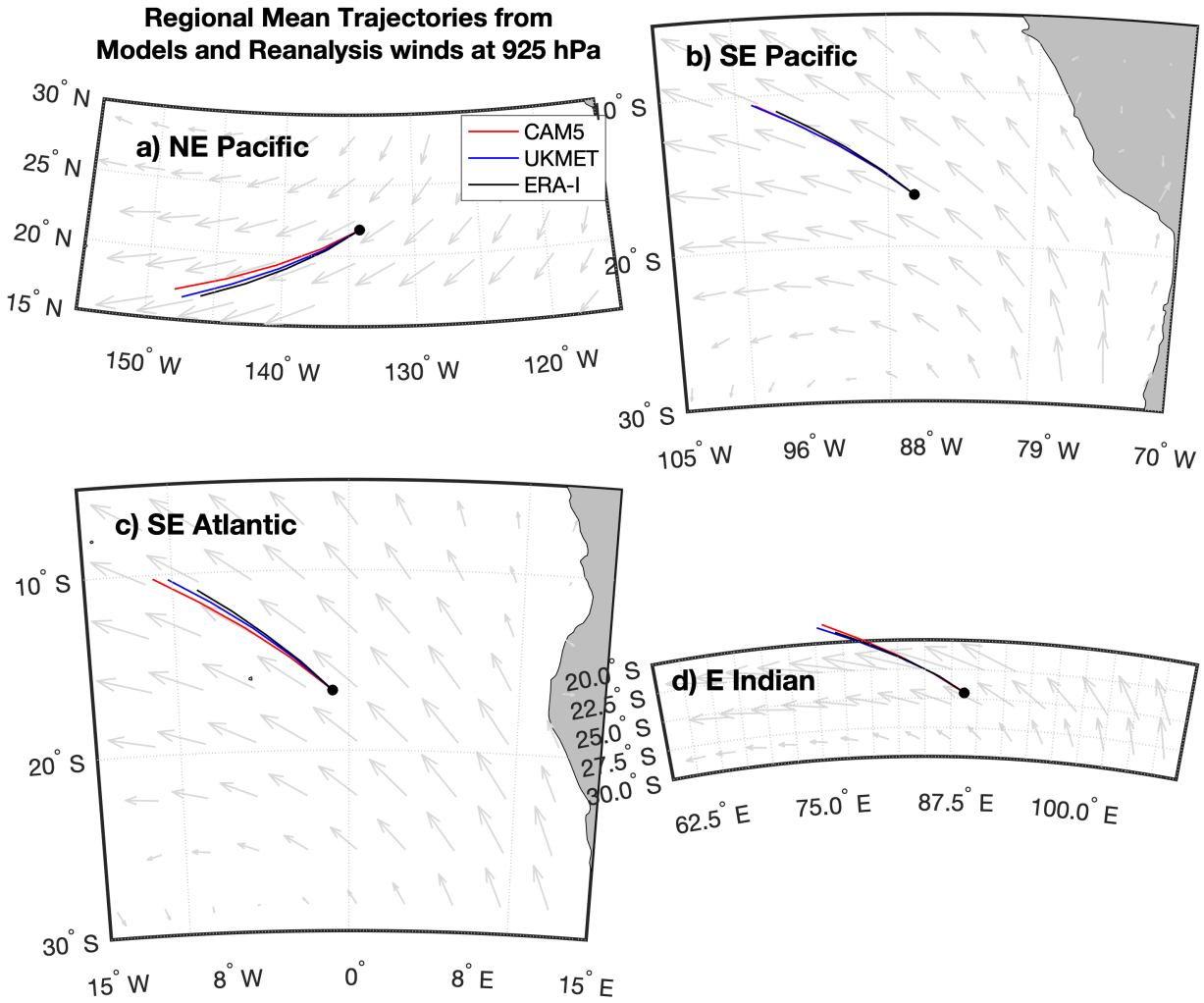

Figure 1. Composited mean forward-running trajectories from the CAM5 (red), UKMET (blue), and ERA-Interim (black) compared for a single 'launch point' for our four study regions: a) the NE Pacific, b) the SE Pacific, c) the SE Atlantic, and d) the E Indian Ocean. Trajectory beginnings are shown as black circles. Trajectories are all generated using the isobaric wind field at 925 hPa and run forward for 48 hours. Mean wind arrows, shown in gray, are based on the 925 hPa wind field from the ERA-Interim.

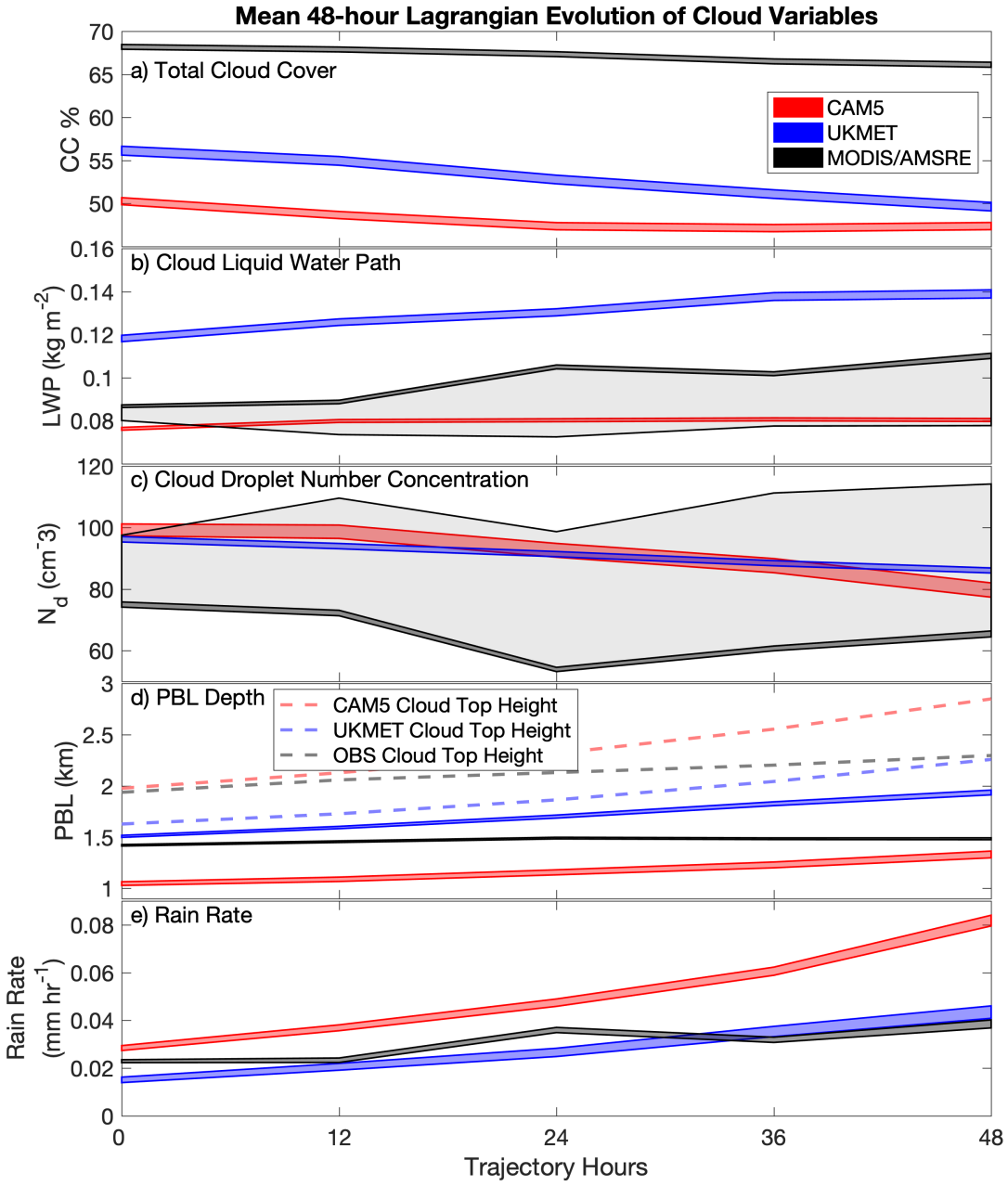

Figure 2. The mean 48-hour evolution of our cloud variables: a) cloud cover, b) in-cloud liquid water path, c) droplet number concentration, d) planetary boundary layer depth, and e) rain rate. Means are generated by compositing all available trajectories from all available regions. The (vertical) width of the lines represents the 2σ standard error of the mean. Frame d shows PBL depth along with an estimate of maximum cloud top height based on the highest clouds in models and coldest clouds in the observations. The light gray error bounds in frames b and c represent the multi-sensor variability in CLWP and N_d.

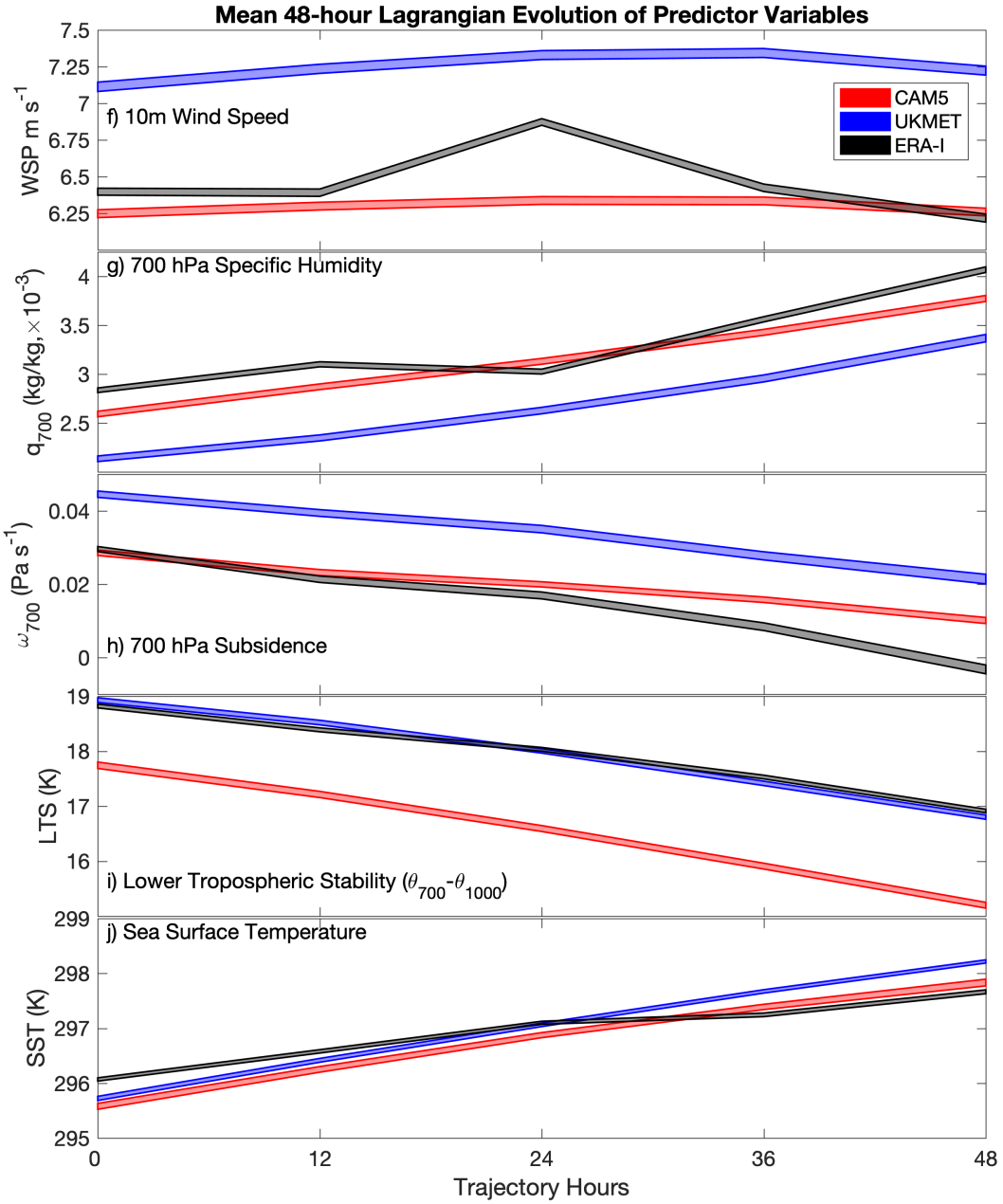

Figure 3. The mean 48-hour evolution of our meteorological predictor variables: f) 10-meter wind speed, g) specific humidity (q) at 700 hPa, h) subsidence at 700 hPa (pressure velocity, ω), i) lower tropospheric stability (the difference in potential temperature, θ, between 700 and 1000 hPa), and j) rain rate. Means are generated by compositing all available trajectories from all available regions. The (vertical) width of the lines represents the 2σ standard error of the mean.

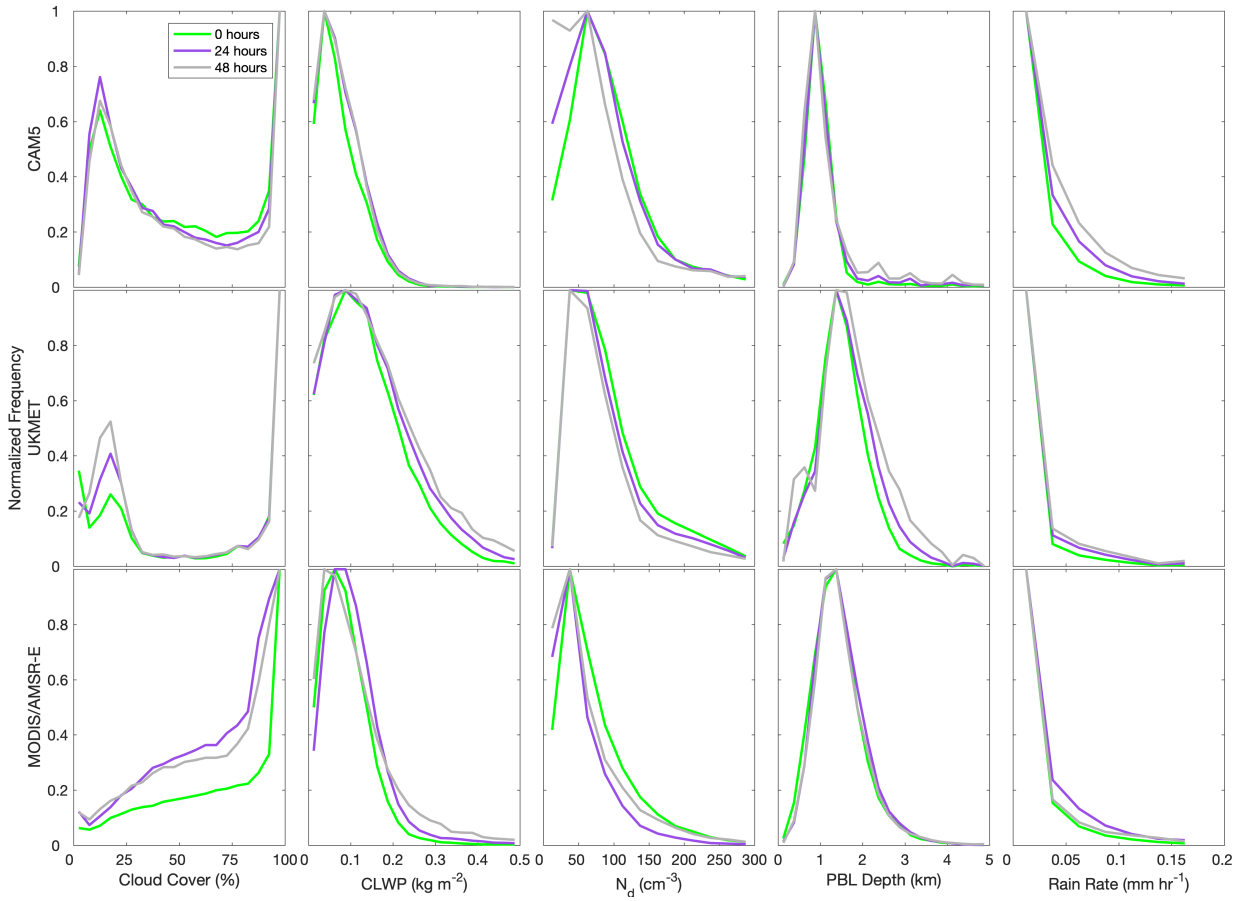

Figure 4. Normalized frequency distributions of our cloud variables shown for three time steps: 0-hours, 24-hours, and 48-hours for all three platforms. Distributions are generated based on all available observations at those time steps.

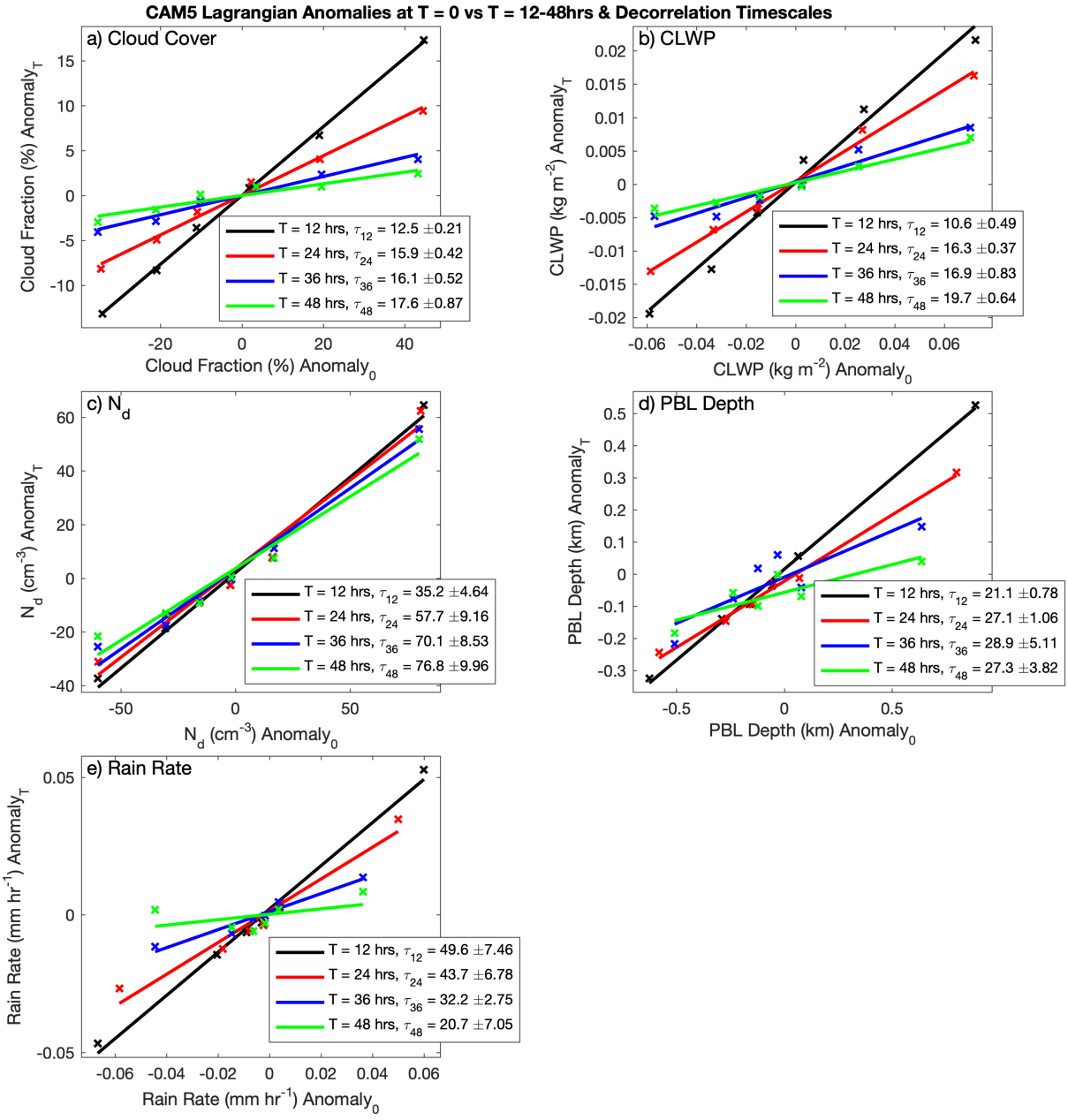

Figure 5. CAM5 cloud variable anomalies at times T (y-axis) as a function of the 0-hour anomaly (x-axis) for six bins of trajectories selected to have equal numbers of observations and binned by 0-hour values. E-folding times (τ) are calculated based on lines fit to the plots using a least squares linear regression and equation 3.

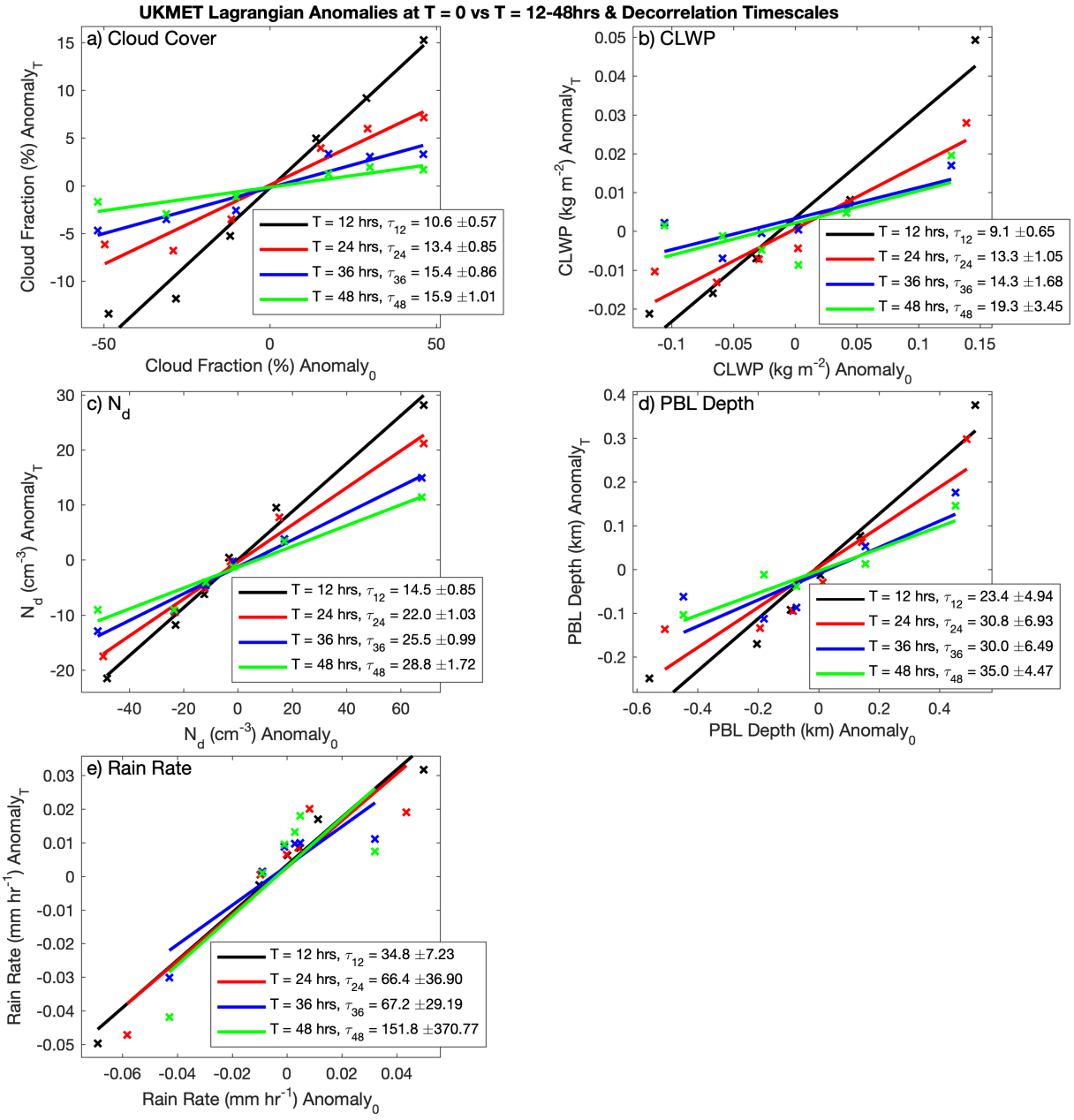

Figure 6. UKMET cloud variable anomalies at times T (y-axis) as a function of the 0-hour anomaly (x-axis) for six bins of trajectories selected to have equal numbers of observations and binned by 0-hour values. E-folding times (τ) are calculated based on lines fit to the plots using a least squares linear regression and equation 3.

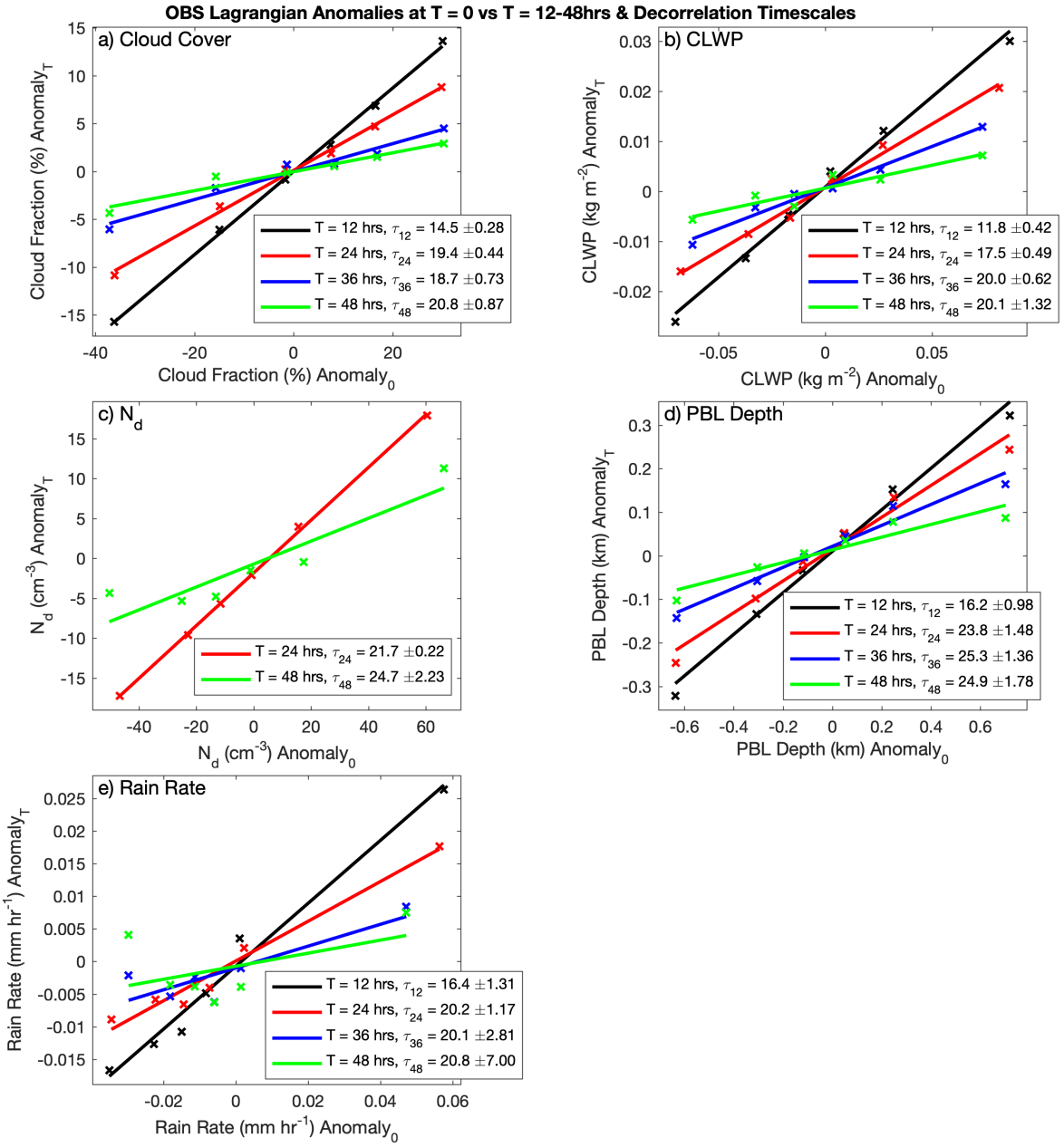

Figure 7. Observed cloud variable anomalies at times T (y-axis) as a function of the 0-hour anomaly (x-axis) for six bins of trajectories selected to have equal numbers of observations and binned by 0-hour values. E-folding times (τ) are calculated based on lines fit to the plots using a least squares linear regression and equation 3.

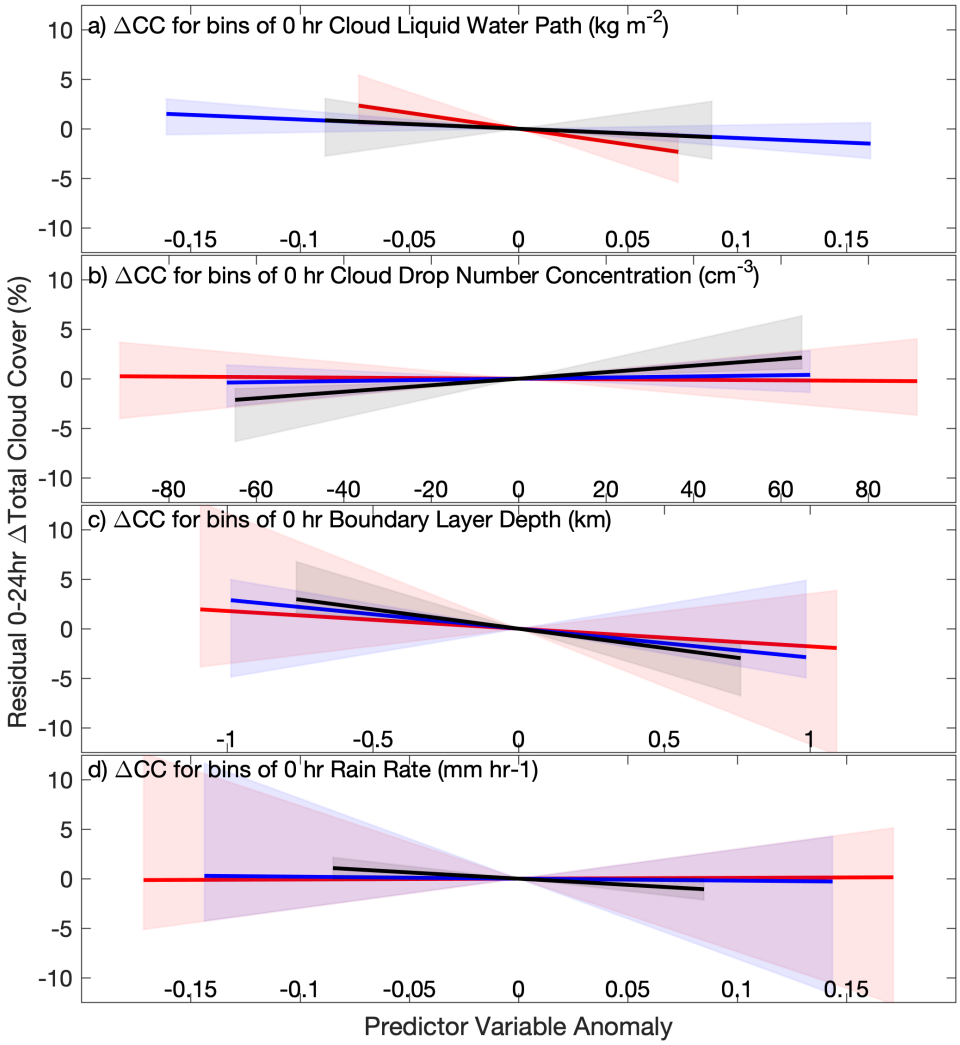

Figure 8. Lines fit to plots of residual cloud cover change as a function of σ-bins of predictor variables, in this case other cloud variables are used as predictors. Lines are generated while holding each of the other predictor variables (both cloud and meteorological) constant. The shaded regions represent the range of slopes produced by holding the predictors constant. Color coding is the same as in previous figures: CAM5 is red, UKMET is blue, and Observations are black.

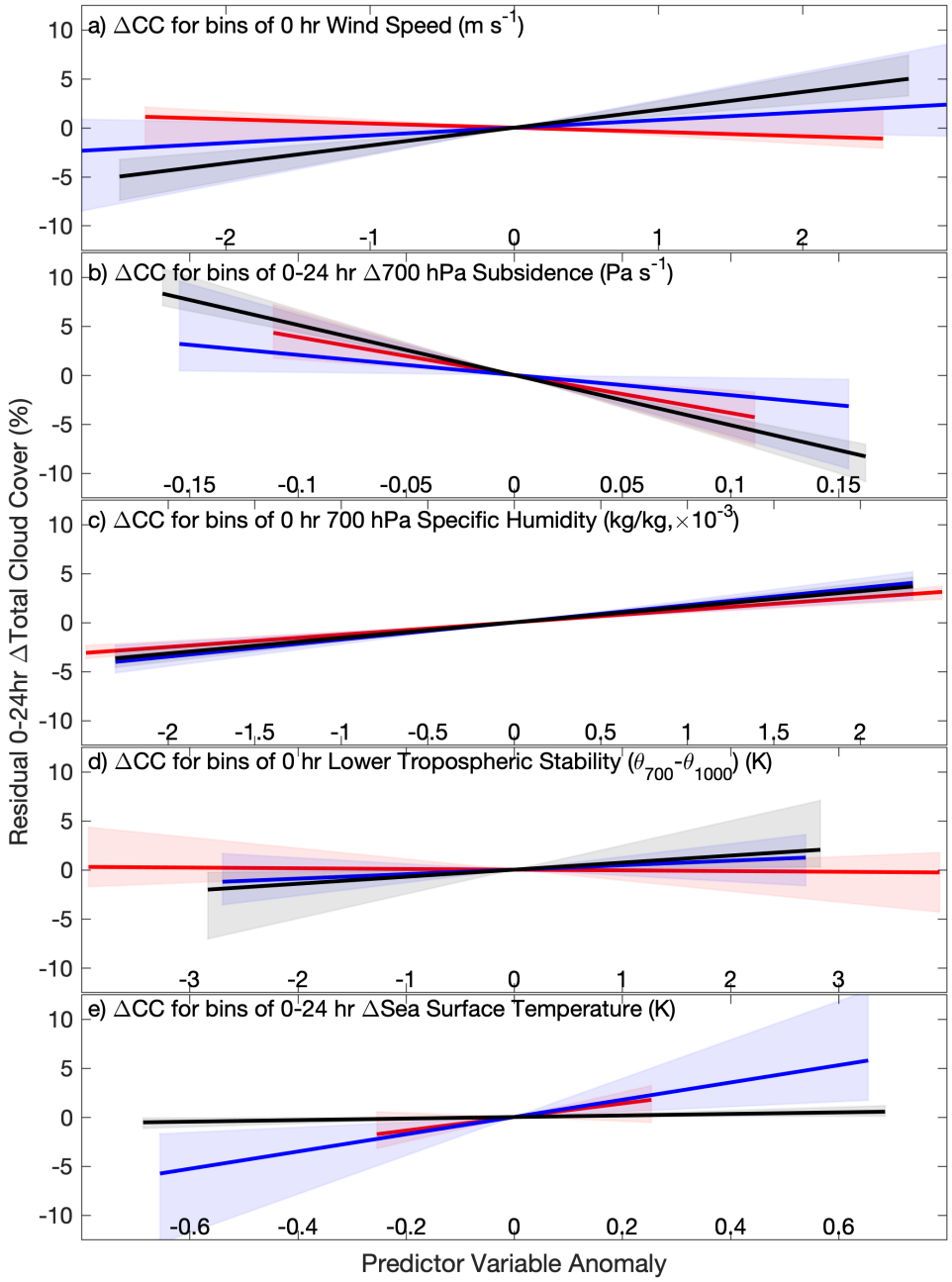

Figure 9. Lines fit to plots of residual cloud cover change as a function of σ-bins of predictor variables, with meteorological variables external to the cloud deck used as predictors here. Lines are generated while holding each of the other predictor variables (both cloud and meteorological) constant. The shaded regions represent the range of slopes produced by holding the predictors constant. Color coding is the same as in previous figures: CAM5 is red, UKMET is blue, and Observations are black.

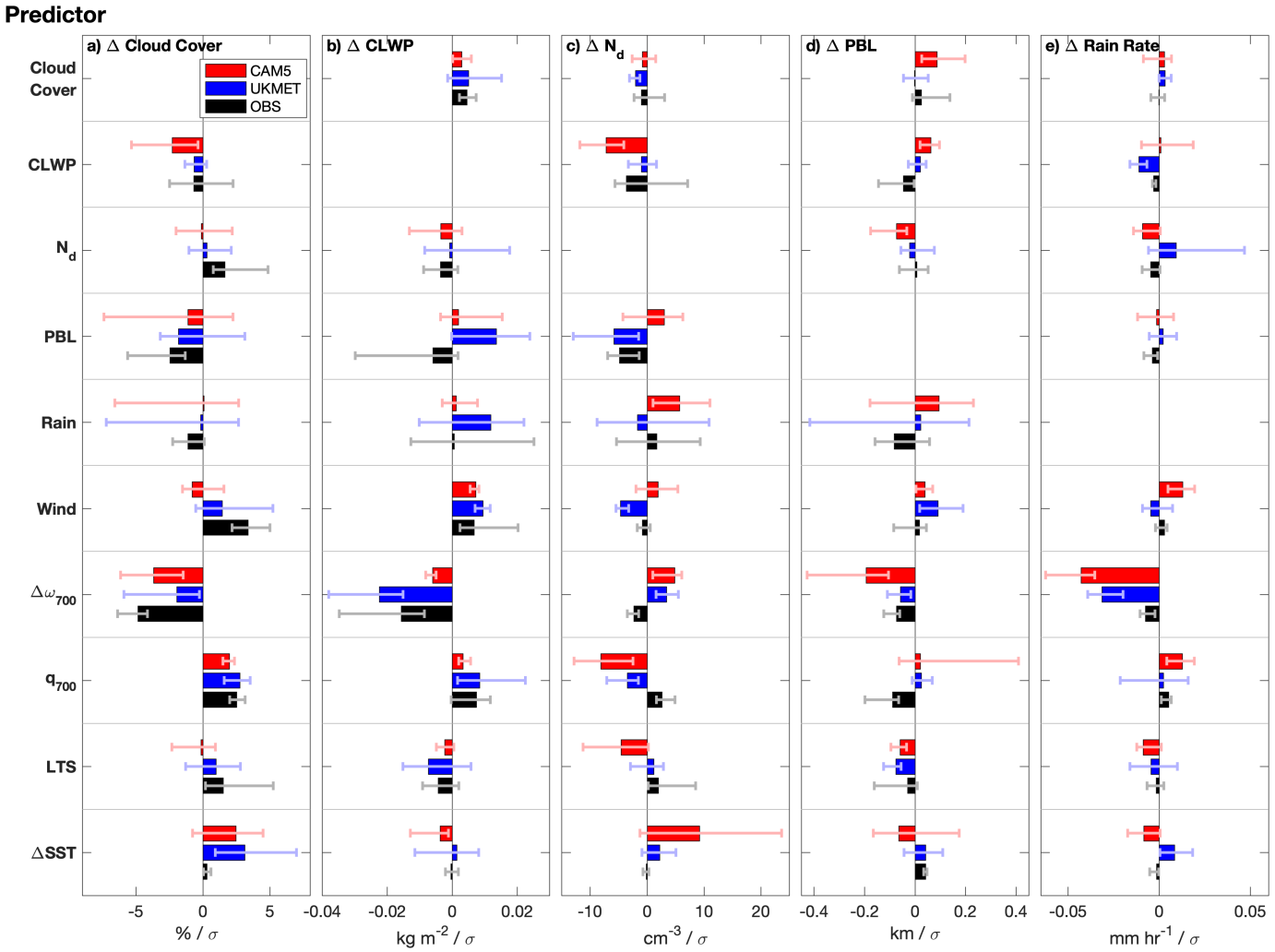

Figure 10. Bar plots representing slopes as shown in Figures 8 and 9, with error bars representing the range of slopes shown by the shaded regions of Figures 8 and 9. Columns of plots are shown for: a) cloud cover, b) in-cloud liquid water path, c) cloud drop concentration, d) planetary boundary layer depth, and e) rain rates. Bars extending to the right indicate a positive cloud variable response to a 1-σ positive deviation of that predictor variable. Values of σ are constant between the platforms for each predictor, allowing for improved comparability.